Orbital Magnetic Moment and Single-Ion Magnetic Anisotropy of the S = 1/2 K 3 [Fe(CN) 6] Compound: A Case Where the Orbital Magnetic Moment Dominates the Spin Magnetic Moment

Marius Retegan, Sadaf Fatima Jafri, Leonardo Curti, Laurent Lisnard, Edwige Otero, Eric Rivière, Maurits W Haverkort, Anne Bleuzen, Ph. Sainctavit, Marie-Anne Arrio

Orbital magnetic moment and single-ion magnetic anisotropy of the $S = 1/2$ $K_3[Fe(CN)_6]$ compound: a case where the orbital magnetic moment dominates the spin magnetic moment.

Marius Retegan,[†] Sadaf Fatima Jafri,[‡,#] Leonardo Curti,[¶] Laurent Lisnard,[¶] Edwige Otero,[§] Eric Rivière,[‖] Maurits W. Haverkort,[⊥] Anne Bleuzen,[‖] Philippe Sainctavit,[‡,§] and Marie-Anne Arrio[*,‡]

†European Synchrotron Radiation Facility, BP 220, F-38043 Grenoble, France.

‡CNRS, Sorbonne Université, Institut de Minéralogie, de Physique des Matériaux et de Cosmochimie, UMR7590, CNRS/SU/IRD/MNHN, 75252 Paris Cedex 05, France

¶Sorbonne Université, CNRS, Institut Parisien de Chimie Moléculaire, FR2769, 75252 Paris Cedex 05, France

§Synchrotron SOLEIL, L'Orme des Merisiers, F-91192 Saint-Aubin, France

‖Institut de Chimie Moléculaire et des Matériaux d'Orsay, Université Paris-Saclay, CNRS, ICMMO, 91405 Orsay cedex

⊥Heidelberg University, Institute for Theoretical Physics, Philosophenweg 19, 69120 Heidelberg, Germany

#Department of Physics, University of Karachi, Karachi, Pakistan

E-mail: marie-anne.arrio@sorbonne-universite.fr

Abstract

The potassium hexacyanoferrate(III), $K_3[Fe^{III}(CN)_6]$, is known for its exceptional magnetic anisotropy among the $3d$ transition metal series. The Fe(III) ions are in the $S = 1/2$ low spin state imposed by the strong crystal field of the cyanido ligands. A large orbital magnetic moment is expected from previous publications. In the present work, X-ray magnetic circular dichroism was recorded for a powder sample, allowing direct measurement of the Fe(III) orbital magnetic moment. A combination of molecular multiconfigurational *ab initio* and atomic ligand field multiplets calculations provides the spin and orbital magnetic moments for the $Fe(CN)_6$ isolated cluster, the crystallographic unit cell and the powder sample. The calculations of the angular dependencies of the spin and orbital magnetic moments with the external magnetic induction direction reveal easy magnetization axes for each $S = 1/2$ $Fe(CN)_6$ molecular entity and the crystal. It also reveals that the orbital magnetic moment dominates the spin magnetic moment for all directions. Our measurements reveal that the orbital magnetic moment contributes 60% of the total magnetization for the powder, in excellent agreement with our theoretical predictions. An orbital magnetic moment greater than the spin magnetic moment is exceptional for $3d$ transition metal ions. The impact of crystal field strength and distortion, π back-bonding, spin-orbit coupling, and external magnetic induction were analyzed, leading to a deeper understanding of the spin and orbital magnetic anisotropies.

1 Introduction

Ferricyanide (or potassium hexacyanoferrate(III), $K_3[Fe^{III}(CN)_6]$) has been known for several centuries and is used in a wide range of domains such as chemistry, physical-chemistry [1–3] and biology. [4,5] It is an ingredient in the synthesis of the famous *Prussian blue*, $Fe_4^{III}[Fe^{II}(CN)_6]$. [6] The $[Fe(CN)_6]^{3-}/[Fe(CN)_6]^{4-}$ redox couple is a standard in electrochemistry where it can be used in analytical chemistry or as an electrolyte for the battery industry. [7,8] The redox properties are widely used in the design of thermo- and photo-magnetic CoFe Prussian blue analogs

and derivative molecular compounds where an electron transfer occurs between Fe(III) and Co^{II} transforming the paramagnetic $Co^{II}-NC-Fe^{III}$ pairs into diamagnetic $Co^{III}-NC-Fe^{II}$ pairs and reversely.[9–15]

The cyanido ligand (CN^-) forms a highly covalent bond with the $3d$ metal ion. The $Fe^{III}-CN$ bond results from the synergy of the σ donor interactions between occupied ligand orbitals with the partially occupied metal orbitals, and the π back-bonding acceptor interactions between the partly occupied metal orbitals and the unoccupied ligand orbitals. The ligands create a large ligand field that dominates the Coulomb electron-electron repulsions so that the Fe(III) ion is in the low spin state *i.e* the $t_{2g}^5 e_g^0$ configuration with $S = 1/2$. The corresponding spectroscopic term for the ground state is $^2T_{2g}$ in O_h symmetry (Schönflies notations).[16] The orbital part with symmetry T_{2g} is the sign of an expected significant angular orbital momentum for the ground state.

Ferricyanide is also known for its peculiar anisotropic magnetic properties, representing an exception among the $3d$ transition metal ion series. The first susceptibility measurements performed in 1933 pointed to the unusual anisotropic behavior.[17] Later electron paramagnetic resonance (EPR) magnetic measurements confirmed the result.[18–25] In the eighties, spin-polarized neutron diffraction (PND) was applied to the understanding of the magnetic properties of $Cs_2K[Fe(CN)_6]$ single crystals, with special attention to the angular dependence of magnetization.[26] From a simple crystal field model, the authors estimated that the orbital magnetic moment contributes 60% of the total magnetization, thus dominating the spin magnetic moment, an exception among the $3d$ transition metal ions.

The recent developments of high-resolution spectroscopic experiments on synchrotron beamlines offered the possibility to probe electronic properties through X-ray absorption spectroscopy (XAS), X-ray emission spectroscopy (XES), and resonant inelastic X-ray scattering (RIXS).[27–29] The magnetic properties can be probed by X-ray magnetic circular dichroism (XMCD), X-ray magnetic linear dichroism (XMLD), and RIXS-MCD. XAS at $L_{2,3}$ edges of $3d$ ions corresponds mainly to transitions between the $2p$ core levels and the

empty $3d$ levels so that it directly probes the electronic properties of the $3d$ levels.[27] In addition, XMCD at $L_{2,3}$ edges is a technique that directly yields the $3d$ orbital magnetic moment thanks to the orbital magneto-optical sum rule and possibly the spin magnetic moment when the spin magneto-optical sum rule holds.[30–32]

As with most other spectroscopies, theoretical calculations provide an essential tool to increase the understanding of the experimental results. The strong electron-electron repulsions and the correlations of the open shell $3d$ elements have to be considered for a correct description. In early works, crystal field multiplet (CFM) and ligand field multiplet (LFM) models were used to interpret susceptibility measurements. Figgis and coworkers proposed an advanced LFM model to calculate the effective magnetic moment of $K_3[Fe^{III}(CN)_6]$.[16,21] Due to computing limitations, the model relied on perturbation theory. Today's LFM models include spin-orbit coupling and configuration interaction and are implemented with full Hamiltonian diagonalization.[33–35] In the case of core spectroscopies, B.T. Thole developed a multi-electronic single-ion model with configuration interactions to account for charge transfer between the ion and the ligands due to the chemical bond.[27,34,36] Special attention was given to calculating the excited states in the presence of the core hole and to transitions between the initial state and the core-hole excited states. For instance, for the X-ray absorption at $L_{2,3}$ edges, the $2p$ core hole created in the excited states yields a strong spin-orbit splitting responsible for the separation of the L_3 and L_2 edges, Coulomb repulsions between $2p$ and $3d$ electrons, while the extra $3d$ electron modifies Coulomb repulsions on the $3d$ shell. All these effects have to be included in the calculation of core spectroscopies to obtain a correct description of the electronic structure and the transition intensities. Indeed, the LFM model was successfully used to calculate XAS and XMCD spectra at $L_{2,3}$ edges of transition metal ions, even for highly covalent bonds.[27,33,34,36–39]

The LFM models are, however, semi-empirical, and require parameters to describe the inter- and intra-atomic interactions. Attempts have been made to circumvent these limitations by using density functional theory (DFT),[40–47] and multiconfigurational*ab initio*

methods to directly calculate the X-ray absorption spectra.[48–53] Recently, Maganas *et al.* have extended the use *ab initio*-based approaches to the calculation of the XMCD spectra of V^{IV} and V^{III} complexes.[54] Although exciting, the use of parameters-free theoretical methods comes with the drawback that they are computationally very demanding. A compromise is to use semi-empirical multiplet approaches to perform the spectroscopy calculations while relying on DFT or *ab initio* calculations to estimate the values of the required parameters. In magnetism, a similar approach is often applied to calculate the spin Hamiltonian parameters used to interpret magnetic measurements such as EPR and SQUID magnetometry.[55]

X-ray spectroscopies have previously been employed in the study of ferricyanide and its related Prussian blue analogs, enabling the determination of electronic and magnetic properties of the $3d$ transition metal ions.[10,12,37–39,56–62] X-ray absorption at the iron $L_{2,3}$ edge was first used by Hocking *et al.* to determine the electronic structure of $K_3[Fe^{III}(CN)_6]$.[39] The experimental measurements were interpreted using LFM calculations. The authors determined the initial state electronic configuration and the charge transfer associated with the metal-cyanido bond (π back-bonding and σ donation).[39] More recently, the electronic properties of $K_3[Fe^{III}(CN)_6]$ and other low-spin Fe(III) complexes were investigated using RIXS measurements, and interpreted using second-order perturbation theory restricted active space (RASPT2).[58] Hahn *et al.* have calculated the electronic structure of $K_3[Fe^{III}(CN)_6]$ within the complete active space self-consistent field (CASSCF) and multireference N-electron valence state perturbation theory (NEVPT2) framework, from which they extracted the ligand field parameters that were subsequently injected into the LFM model to calculate $2p3d$ RIXS maps.[60]

In the present work, we study the local magnetic properties of a powder sample of $K_3[Fe^{III}(CN)_6]$. We use XMCD to measure the Fe(III) orbital magnetic moment, and SQUID magnetometry for the total magnetization. The experiments are performed at 2 K and 6.5 T, making the magnetization close to the saturation limit. We compare the results with two other low spin Fe(III) compounds: (i) $(N(C_4H_9)_4)[TpFe^{III}(CN)_3]$ (where Tp is tris-pyrazolyl

borate ligand) for which XMCD interpreted by LFM was previously published.[32] In this compound Fe(III) is coordinated by three cyanido ligands and three nitrogen atoms of Tp. The compound is labelled $Fe^{III}Tp$ in the following. (ii) The ferric bis(1,4,7-triazacyclononane) chloride complex, $[Fe(tacn)_2]Cl_3 \cdot 5\,H_2O$, where Fe(III) is coordinated by six nitrogen from two tacn ligands, and the bonding does not involve π back-donation. This compound is labelled $Fe^{III}(tacn)_2$ in the following.

The interpretation of XAS and XMCD measurements was carried out using LFM calculations. The required parameters of the initial Hamiltonian were extracted from multiconfigurational *ab initio* calculations. The magnetization curves and the expectation values of the spin and orbital magnetic moments were obtained using the same *ab initio* methods. Particular attention was paid to the angular averaging of the calculated quantities, as required by the fact that the measurements are performed on powder samples. We analyze the behavior of the spin magnetic moment with respect to the orbital magnetic moment, by examining the effect of the crystal field symmetry, spin-orbit coupling, and hybridization. The present work allows us to identify the key parameters responsible for the magnetic anisotropy.

2 Methods

2.1 Materials and SQUID magnetic measurements

Potassium hexacyanoferrate(III), $K_3[Fe^{III}(CN)_6]$, was purchased from Sigma-Aldrich and used without further purification. The ferric bis(1,4,7-triazacyclononane) chloride complex, $[Fe(tacn)_2]Cl_3 \cdot 5\,H_2O$, was prepared adapting reported procedures.[60,63,64] $FeCl_3 \cdot 6\,H_2O$ (0.056g, 0.21 mmol) was dissolved in DMSO (2 mL), heated to 140 °C, and left to cool down to room temperature. H_3tacn (0.100 g, 0.42 mmol) in 96% EtOH (2 mL) was treated with an ethanolic 1 M solution of KOH (3eq. 1.26 mL) and added drop-wise under stirring to the Fe(III) solution. The formed yellow precipitate was removed by centrifugation, and the resulting solution was placed in a sand bath at 60 °C. Prismatic orange crystals of

$[Fe(tacn)_2]Cl_3 \cdot 5\,H_2O$ form within 12 hours.

Magnetic properties were investigated using a Quantum Design XL-7 SQUID magnetometer. 34 mg of grinded $K_3[Fe^{III}(CN)_6]$ were pressed into a pellet and placed in a straw in the magnetometer. The dependence of magnetization was recorded at 2 K, 4 K and 10 K for a magnetic induction varying between -6.5 T and 6.5 T. The diamagnetic correction was estimated using Pascal's constants, and the magnetic data were corrected for the diamagnetic contributions of the sample holder.

2.2 XAS and XMCD experiments

The powder sample was deposited on a double-sided conductive carbon tape suitable for cryogenic temperatures and mounted on a copper sample holder. XAS and XMCD measurements were recorded at Fe $L_{2,3}$ edges ($2p \rightarrow 3d$) on DEIMOS beamline (SOLEIL synchrotron, France)[65] in total electron yield (TEY) under ultra-high vacuum conditions. XMCD spectra were recorded at 2 K and 6.5 T.

To avoid any spurious signals, the XMCD was measured by taking the difference of two XAS spectra recorded for left and right polarized X-rays with the external magnetic induction parallel (B^+) or antiparallel (B^-) to the X-ray propagation vector. By definition, the XMCD signal is obtained by $\sigma_{\mathrm{XMCD}} = \sigma^- - \sigma^+$ where $\sigma^- = [\sigma_L(B^-) + \sigma_R(B^+)]/2$ and $\sigma^+ = [\sigma_L(B^+) + \sigma_R(B^-)]/2$. The XAS is defined by $\sigma_{\mathrm{XAS}} = \frac{1}{2}(\sigma^- + \sigma^+)$.

The orbital magnetic moment is obtained by applying the sum rules[30,31] to the XAS/XMCD spectra. The background was subtracted from the XAS spectrum using two arctangent functions that model the $2p_{3/2} \rightarrow$ continuum and $2p_{1/2} \rightarrow$ continuum transitions.[66] The XAS is normalized to 1 at the maximum close to 710 eV and the XMCD is expressed as a percentage of this maximum. The spin sum rule cannot be applied in the case of low spin Fe^{III} due to the strong intermixing between L_3 and L_2.[32]

XMCD-detected magnetization curves were measured as a function of the applied magnetic induction. The monochromator was set at the energy of the maximum intensity (in

absolute value) of the XMCD signal. The XMCD intensity was measured by sweeping the intensity of the external magnetic induction between +6.5 T and -6.5 T and flipping the circular polarization at each induction step. The XMCD-detected magnetization curves were recorded at 2 K and 10 K.

2.3 Multiconfigurational *ab initio* calculations

We have performed cluster model calculations for both $K_3[Fe^{III}(CN)_6]$ and $Fe^{III}Tp$. The $K_3[Fe^{III}(CN)_6]$ model was constructed starting from the experimental X-ray diffraction structure ($P2_1/n$ space group, #14),[67] and includes the iron atom and the six coordinating cyanide ligands. The unit cell contains four different Fe(III) ions and we selected the cluster around the Fe(III) ion with Cartesian coordinates $(3.460, 0.106, -0.013)$, labeled 1 in Figure 1. The coordinates of the $Fe(CN)_6$ cluster are given in Supplementary Information (S1). In the following, all coordinates are given in the $\{\hat{x}, \hat{y}, \hat{z}\}$ orthonormal frame where the $\{\hat{a}, \hat{b}, \hat{c}\}$ cell frame is defined by: $\hat{a} = (14.021, 0, 0), \hat{b} = (0, 10.401, 0), \hat{c} = (-2.467, 0, 7.966)$ (in Å). The $Fe^{III}Tp$ coordinates were taken from the work of Ridier and coworkers.[55]

In the case of $K_3[Fe^{III}(CN)_6]$, we have also performed embedded cluster calculations. The array of point charges surrounding the quantum cluster was generated using the Ewald program[68] from a 4 x 6 x 8 supercell. In total, 13811 point charges were considered. The initial values of the charges were set to 0.9, -0.8, 0.4, and 0.5 for Fe, N, C, and K, respectively. A spherical region around the quantum cluster containing 487 point charges was kept to the set values. The remaining charge array was optimized to reproduce the electrostatic potential of the infinite crystal.[69] To limit the unphysical overpolarization effects of the quantum cluster by the array, 34 of the neighboring point charges were capped with effective core potentials. We used the ECP2MWB for nitrogen and carbon,[70] and ECP10MWB for potassium.[71]

The point group symmetry of iron in $K_3[Fe^{III}(CN)_6]$ is C_1. In addition to the calculations presented above, we have also performed calculations of the symmetrized $K_3[Fe^{III}(CN)_6]$

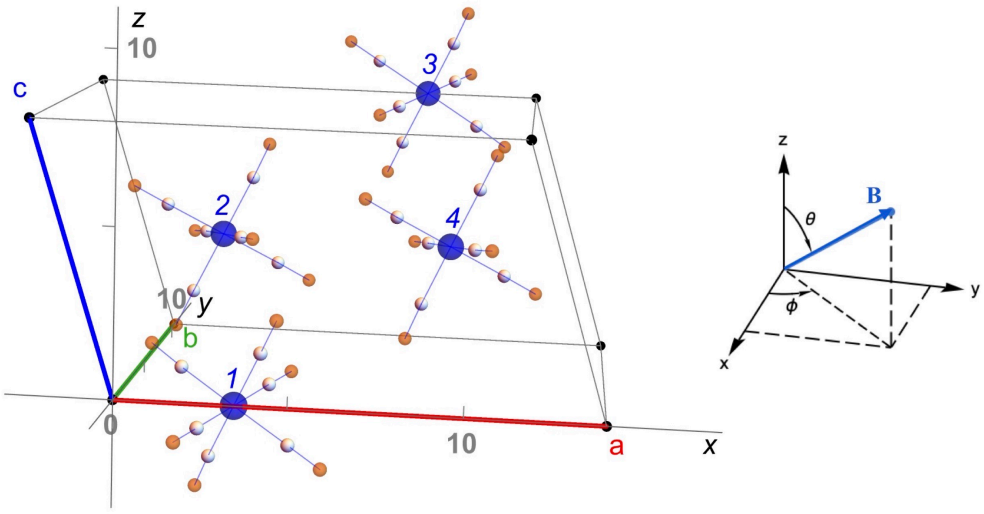

Figure 1: (Left) Representation of the four Fe(III) sites in the crystal unit cell of $K_3[Fe^{III}(CN)_6]$.[67] Fe(III) ions in blue, C atoms in grey and N atoms in orange. The K^+ ions are omitted. Each Fe(III) site is labeled from 1 to 4. The $\{a, b, c\}$ cell frame is colored: a in red, b in green, and c in blue. The $\{\hat{x}, \hat{y}, \hat{z}\}$ frame is in black. Units are Å. (Right) Coordinates of the magnetic induction **B** in this frame.

cluster model with the C_{3v}, D_{4h}, and O_h point group symmetries. The Cartesian coordinates were obtained using the automatic point group determination procedure from the ChemCraft visualization program.[72] For each symmetry, we have selected the structure with the lowest root-mean-square displacement (RMSD) of the atomic positions.

All calculations were performed using the Orca software package.[73] The starting orbitals for the correlated multiconfigurational *ab initio* calculations were the quasi-restricted orbitals obtained from a DFT calculation. We used the PBE density functional,[74] the relativistically contracted version[75] of the def2-TZVP basis set,[76] and the corresponding fully decontracted auxiliary basis set[77] for the resolution of identity. Scalar relativistic effects were introduced using the Douglas-Kroll-Hess (DKH) approach.[78]

The complete active space self-consistent field (CASSCF) calculations were done using the same basis sets and scalar relativistic treatment as in the DFT calculations. We used

two active space sizes in the calculations. The smaller one included the 5 electrons in the $3d$ orbitals of iron, denoted in the following (5,5). The second larger one included, in addition, two σ bounding orbitals containing 4 electrons and the empty $4d$ orbitals, resulting in a total of 9 electrons distributed over 12 orbitals, or (9,12). The larger active space has been shown previously to provide converged results for the magnetic properties of $Fe^{III}Tp$.[55] The orbital energies, Slater F^k integrals, and the spin-orbit coupling constant (ζ_{3d}) were calculated using the smaller active space of the $3d$ orbitals alone using the *ab initio* ligand field theory.[79] In these calculations, we considered all possible excited states within the active space, i.e., 1 sextet, 24 quartets, and 75 doublets. The use of the smaller active space is required by the *ab initio* ligand field (AILFT) procedure as the energies and eigenvectors of all calculated states are fitted to an analytical ligand field Hamiltonian, which by definition include only the $3d$ metal orbitals. For all other properties, i.e., magnetization curves and expectation values, we only included 1 sextet, 6 quartets, and 12 doublets states, regardless of the active space size. Dynamical electron correlation was introduced on top of the CASSCF wave functions employing the N-electron valence state perturbation theory (NEVPT2).[80,81] If not specified otherwise, all reported values include the NEVPT2 correction.

Spin-orbit coupling (SOC) was introduced using the quasi-degenerate perturbation theory (QDPT). In this approach, the matrix elements of a mean-field representation of the SOC operator[82] are calculated for the non-relativistic states, with the spin quantum number S and spin projection quantum number M_S. The matrix elements for the remaining terms of the multiplet are generated using the Wigner-Eckart theorem. The SOC matrix is then added to the Born-Oppenheimer Hamiltonian, and the resulting matrix is diagonalized to yield the SOC states. The effect of the magnetic induction is accounted for in a similar way, i.e., by adding the matrix elements of the Zeeman Hamiltonian to the resulting matrix before the diagonalization. In the following, for the analysis of the electronic and magnetic structures, we used the CASSCF/NEVPT2(9,12) calculation.

2.4 Ligand field multiplet calculations

Ligand field multiplet (LFM) calculations were performed using Quanty library [40,83,84] through the graphical user interface Crispy. [85] The parameters for the spherical part of the LFM Hamiltonian, *i.e.* the Coulomb integrals F^k and the $3d$ spin-orbit coupling constant ζ_{3d} were taken starting from the multiconfigurational *ab initio* calculation.

The exact point group symmetry for Fe^{III} in $K_3[Fe^{III}(CN)_6]$ is C_1, where the 6-fold coordinated Fe^{III} ion is sitting in a distorted octahedron with a pseudo 3-fold axis (see Figure 1). The best-suited point group for LFM calculations is C_{3v}. Note that the D_{4h} point group was used in most previous studies of $K_3[Fe^{III}(CN)_6]$ although there is no pseudo 4-fold axis in the crystallographic structure. In C_{3v} symmetry, the crystal field Hamiltonian has three parameters, $10Dq$, $D\sigma$, $D\tau$. [86]

The chemical bond between the Fe^{III} ion and the CN^- ligands is described in terms of σ donation between the occupied orbitals of the ligand and the unoccupied and partially occupied orbitals of the metal, and π back-bonding between the occupied orbitals of the metal ion and the unoccupied orbitals of the ligands. [37,39] In the LFM model, at least three electronic configurations are needed to account for the bonding situation. The σ donation can be modeled by the reduction in electron repulsion (κ) known as the nephelauxetic effect and by the ligand-to-metal charge transfer (LMCT) through the configuration interaction between $|2p^6 3d^5\rangle$ and $|2p^6 3d^6 \underline{L}\rangle$, where $\underline{L}$ stands for one hole in a ligand orbital. The π back-bonding can be modeled by the metal-to-ligand charge transfer (MLCT) through the configuration interaction between $|2p^6 3d^5\rangle$ and $|2p^6 3d^4 L^-\rangle$, where L^- stands for one additional electron on a ligand orbital. In Hocking *et al.*, [39] the initial state of the Fe^{III} ion is a linear combination of the three electronic configurations $|2p^6 3d^5\rangle$, $|2p^6 3d^4 L^-\rangle$, and $|2p^6 3d^6 \underline{L}\rangle$. In the present work, to restrict the number of parameters, we performed configuration interaction calculations using only the two configurations required to account for MLCT. The initial state is expressed as a linear combination $\alpha|2p^6 3d^5\rangle + \beta|2p^6 3d^4 L^-\rangle$, where the charge transfer energy Δ_i is the energy difference between the configurations. The core-hole excited state is

$\alpha|2p^5 3d^6\rangle + \beta|2p^5 3d^5 L^-\rangle$, where the charge transfer energy Δ_f is the energy difference between $|2p^5 3d^6\rangle$ and $|2p^5 3d^5 L^-\rangle$. We established the Hamiltonian for the MLCT in C_{3v} symmetry (also valid for LMCT), where the $t_{2g}(O_h)$ orbitals split into $a_1(C_{3v})$ and $e(C_{3v})$ and the $e_g(O_h)$ transforms as $e(C_{3v})$. The hybridization Hamiltonian is thus separated into three terms (we neglect the mixing between $e(e_g)$ and $e(t_{2g})$):

$$H_{hyb}^{C_{3v}} = H_{hyb}^{e(e_g)} + H_{hyb}^{a_1(t_{2g})} + H_{hyb}^{e(t_{2g})} \tag{1}$$

where:

$$H_{hyb}^{a_1(t_{2g})} = \left(\frac{1}{5}C_0^0 + C_2^0 + \frac{9}{5}C_4^0\right) V_{a_1(t_{2g})} \tag{2}$$

$$H_{hyb}^{e(t_{2g})} = \left(\frac{2}{5}C_0^0 - C_2^0 - \sqrt{\frac{14}{5}}(C_4^{-3} - C_4^3) - \frac{2}{5}C_4^0\right) V_{e(t_{2g})} \tag{3}$$

$$H_{hyb}^{e(e_g)} = \left(\frac{2}{5}C_0^0 + \sqrt{\frac{14}{5}}(C_4^{-3} - C_4^3) - \frac{7}{5}C_4^0\right) V_{e(e_g)} \tag{4}$$

The irreducible representations of the O_h group that are parents of the irreducible representations of the C_{3v} group are indicated in parentheses. The MLCT Hamiltonian has thus four parameters, Δ_i, $V_{e(e_g)}$, $V_{a_1(t_{2g})}$ and $V_{e(t_{2g})}$. The Hamiltonian matrices for crystal field and MLCT in C_{3v} symmetry are provided in SI (Table S7) with the basis set functions (Table S8).

2.5 Powder averages

All experimental data were measured on powder samples. Therefore, to be directly comparable, the calculated magnetic properties and spectra must be averaged over all possible orientations of the external magnetic induction to the crystallographic axes of $K_3[Fe^{III}(CN)_6]$. In all calculations, we chose to fix the local frame of $K_3[Fe^{III}(CN)_6]$ and to rotate the magnetic induction; another possibility would have been to rotate the local axes in a fixed magnetic

induction, but since we are averaging scalar quantities, both methods are equivalent.

The average of a function $f(\theta, \phi)$ defined on the unit sphere, where (θ, ϕ) are the spherical coordinates, is equal to the surface integral of the function divided by the area of the unit sphere:

$$f_{av} = \frac{1}{4\pi} \int f(\Omega)\, \mathrm{d}\Omega = \frac{1}{4\pi} \int_0^{2\pi} \mathrm{d}\phi \int_0^{\pi} f(\phi, \theta) \sin\theta\, \mathrm{d}\theta \tag{5}$$

The Lebedev quadrature transforms the integral into a discrete sum, and the averaged value becomes:

$$\tilde{f}_{av} = \sum_{k=1}^{N} w_k f(\theta_k, \phi_k) \tag{6}$$

where N is the number of grid points, $f(\theta_k, \phi_k)$ is the value of the function at k-th grid point, and w_k is the corresponding weight. For the calculation of the average expectation of an operator $O_{\hat{k}}$, the equation becomes:

$$\langle O_{\hat{k}} \rangle_{av} = \sum_{k=1}^{N} w_{\hat{k}} \sum_{i=1}^{I} p_i \langle O_{\hat{k}} \rangle_i \tag{7}$$

where $O_{\hat{k}} = \sin(\theta_{\hat{k}}) \cos(\phi_{\hat{k}}) O_x + \sin(\theta_{\hat{k}}) \sin(\phi_{\hat{k}}) O_y + \cos(\theta_{\hat{k}}) O_z$ is the operator along the direction $(\theta_{\hat{k}}, \phi_{\hat{k}})$. The expectation values are calculated in all populated relativistic states I at a finite temperature in an external magnetic induction along the direction $(\theta_{\hat{k}}, \phi_{\hat{k}})$. The individual values were averaged using the Boltzmann factors p_i.

We have calculated the average values for the spin and orbit angular momenta using the approach outlined before using both multiconfigurational *ab initio* and LFM methods. The magnetic dipole operator, $\hat{T}_{\hat{k}}$, present in the spin sum rule, has also been calculated with the LFM, but not using the *ab initio* methods as it is not implemented in Orca. The averaged values were subsequently used to calculate the magnetic moments along $\hat{B}$. In units of Bohr magneton, with $\mu_B > 0$, the spin and orbital moments are defined as $\mathcal{M}^{spin}_{powder} = -g_0 \langle S_{\hat{k}} \rangle_{av} / \hbar$ and $\mathcal{M}^{orbit}_{powder} = -\langle L_{\hat{k}} \rangle_{av} / \hbar$, respectively where g_0 is the gyromagnetic factor of the electron

($g_0 \approx 2.002319$).

The method has also been applied to compute the XAS and XMCD theoretical powder spectra, again limited to the LFM method. In the case of cubic symmetry, Ayant et al.[87] derived equations for averaged observables that require only calculating a few magnetic induction directions. However, the method cannot be applied since $K_3[Fe^{III}(CN)_6]$ departs from cubic symmetry. In all calculations, the summation was done using the upper hemisphere of a Lebedev quadrature of order 47, resulting in 385 grid points and associated weights.

3 Results for the powder $K_3[Fe^{III}(CN)_6]$

3.1 Experimental XAS and XMCD at Fe^{III} $L_{2,3}$ edges

The XAS and XMCD spectra at iron $L_{2,3}$ edges for $K_3[Fe^{III}(CN)_6]$ are reported in Figure 2 and compared to those of Fe^{III}Tp (data from reference[32]) and $Fe^{III}(tacn)_2$. In the three compounds, the Fe(III) ion is in the low-spin state and has a distorted octahedral symmetry. The effect of π back-bonding appears in the 711-715 eV region at the L_3 edge and 724-725 eV region at the L_2 edge, as was initially described by Hocking *et al.* for XAS.[39] The XMCD percentage is the ratio between the XMCD signal and the XAS at 709.8 eV.

Applying the orbital magneto-optic sum rule yields $\mathcal{M}^{orbit}_{powder}$ = 0.56 μ_B assuming 5 *d*-electrons (5 holes). The spin sum rule has not been applied since it is not valid for Fe^{III} and even less so for low spin electronic configuration.[32,88] The results are reported in Table 1. Details for the application of the sum rules are given in SI Section S-1.

3.2 Experimental magnetizations

The SQUID-detected magnetization curve at 2 K and 10 K are reported in Figure 3. The X-ray-detected magnetization curve is also reported (Figure 3, right y-scale). It is obtained by setting the monochromator energy at 705.7 eV and scanning the magnetic induction between +6.5 T and -6.5 T. The right and left y-scales were chosen so that both magnetizations at

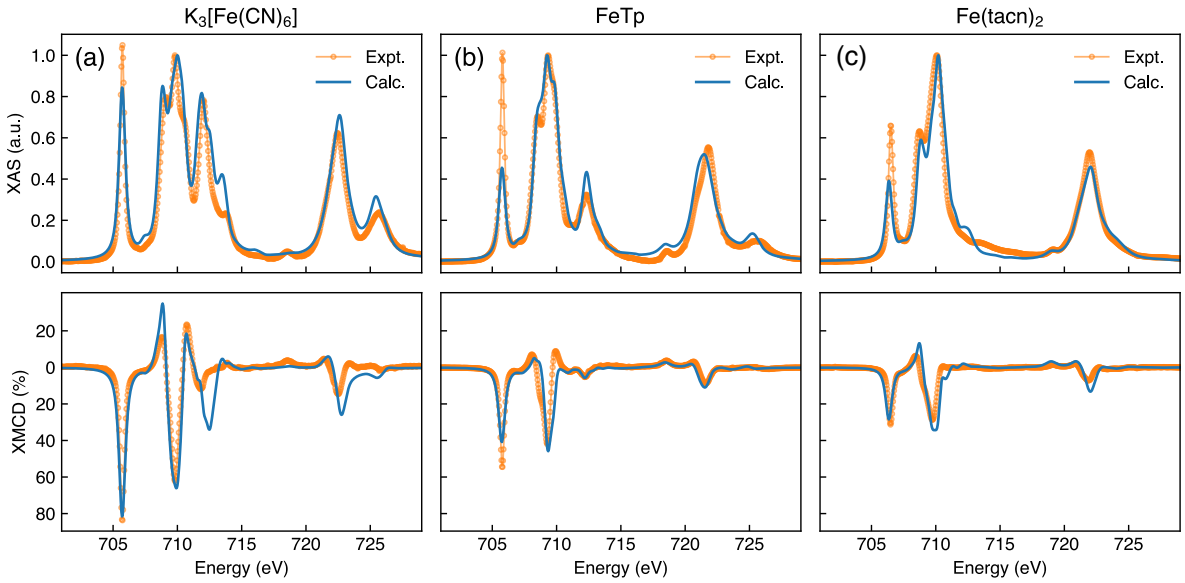

Figure 2: XAS and XMCD spectra at Fe $L_{2,3}$ edges recorded at 2 K and 6.5 T for the three Fe^{III} compounds: (a) $K_3[Fe^{III}(CN)_6]$, (b) $Fe^{III}Tp$ and (c) $Fe^{III}(tacn)_2$. Experiment and LFM calculation for a powder sample.

6.5 T and 2 K superimpose. One can first notice that at both 2 K and 10 K, the magnetization curves superimpose between 0 T and 6.5 T. Secondly, the magnetization is not saturated at 6.5 T and 2 K. At 2 K, the SQUID detected value at 6.5 T is 0.99 μ_B per Fe(III) ion and 0.60 μ_B at 3 T.

3.3 Magnetization from multiconfigurational *ab initio* calculations

The $^2T_{2g}$ ground state in O_h symmetry for low spin Fe(III) ion is split into three Kramer doublets with respective energies at 0 meV, 73 meV, and 105 meV. From the calculations, one can also compute the expectation values $\langle L_{\hat{k}} \rangle$ and $\langle S_{\hat{k}} \rangle$, as defined in section 2.5 and this can be done for any $\hat{k}$ direction. Then for a powder, following the expressions given in section

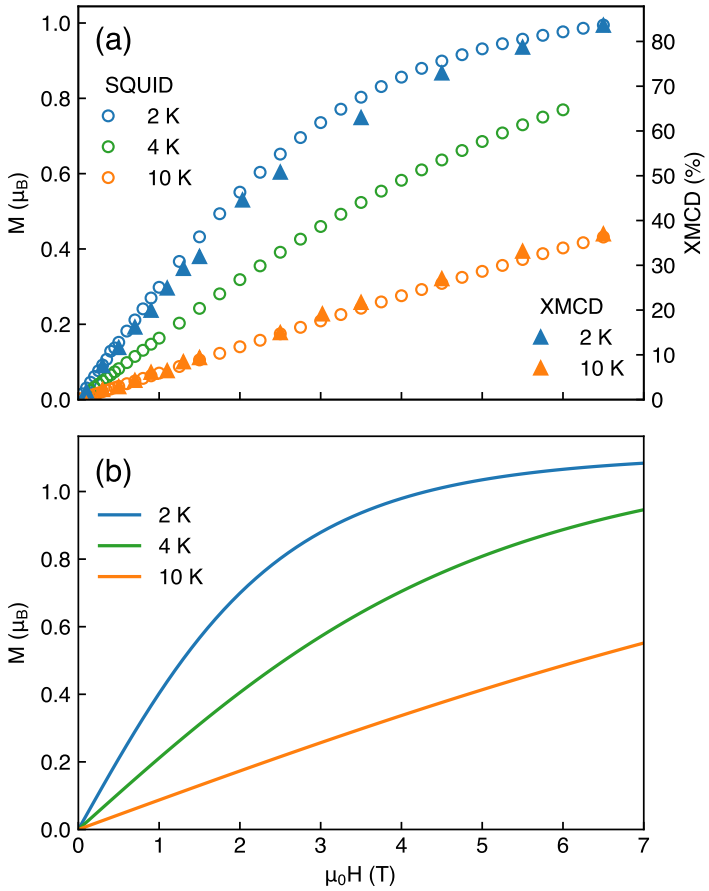

Figure 3: (a) (Left y-axis) Magnetization curve of a $K_3[Fe^{III}(CN)_6]$ powder measured by a SQUID magnetometer at 2 K, 4 K and 10 K. (Right y-axis) Magnetization curve measured by XMCD at 2 K and 10 K. (b) $K_3[Fe^{III}(CN)_6]$ theoretical multiconfigurational *ab initio* magnetization curves, calculated for the powder at 2 K, 4 K and 10 K.

2.5, it is possible to calculate $\langle L_{\hat{k}} \rangle_{powder}$ and $\langle S_{\hat{k}} \rangle_{powder}$ and $\mathcal{M}^{total}_{powder}$ (see Table 1). At 2 K and 6.5 T, $\mathcal{M}^{total}_{powder} = 1.08\mu_B$, well in line though slightly larger than the experimental magnetic moment from SQUID measurements ($0.99\mu_B$). The theoretical magnetizations $\mathcal{M}_{powder}$ were computed at 2 K, 4 K, and 10 K and for magnetic inductions varying between 0 T and 6.5 T (Figure 3).

The multiconfigurational *ab initio* calculations at 6.5 T and 2 K give, for $K_3[Fe^{III}(CN)_6]$, $\mathcal{M}^{spin}_{powder} = 0.39\mu_B$, $\mathcal{M}^{orbit}_{powder} = 0.69\mu_B$ and $\mathcal{M}^{total}_{powder} = 1.08\mu_B$, and for FeTp, $\mathcal{M}^{spin}_{powder} = 0.61\mu_B$, $\mathcal{M}^{orbit}_{powder} = 0.55\mu_B$ and $\mathcal{M}^{total}_{powder} = 1.16\mu_B$. In both cases, the spin magnetic moment is much smaller than $1\mu_B$, contrary to what could have been expected for a pure ($S = 1/2$,

Table 1: Calculated angular momenta and magnetic moments for a $K_3[Fe^{III}(CN)_6]$ powder at 2 K and 6.5 T, compared to experimental XMCD and SQUID magnetometry measurements.

	Calculation		Experiment
	ab initio	LFM	
$g_0\langle S_{\hat{k}}\rangle_{powder}$	−0.39	−0.37	
$\langle L_{\hat{k}}\rangle_{powder}$	−0.69	−0.79	−0.56[a]
$\langle T_{\hat{k}}\rangle_{powder}$		−0.07	
$\mathcal{M}^{total}_{powder}(\mu_B)$	1.08	1.16	0.99[b]

[(a)] from XMCD. [(b)] from SQUID.

$m_S = -1/2$) state and the orbital contribution to the magnetic moment is larger than the spin contribution. This is in line with previous results stating that the orbital magnetic moment is rather large in $K_3[Fe^{III}(CN)_6]$ at the difference with most transition metal ions for which the orbital angular momentum is almost quenched.[89] For $K_3[Fe^{III}(CN)_6]$, the orbital magnetic moment contributes to 64% of the total magnetic moment (57% from our measurements). This result is to be compared with the 60% contribution found by Day *et al.* from their LFM analysis of polarized neutron diffraction experiments.[26]

3.4 XAS/XMCD and magnetic moments from ligand field multiplet calculation

For the initial states ($\alpha|2p^6 3d^5\rangle + \beta|2p^6 3d^4 L^-\rangle$), the Slater integrals (F^k) and spin-orbit integral (ζ_{3d}) were taken from the multiconfigurational *ab initio* calculation. In the core-hole excited states ($\alpha|2p^5 3d^6\rangle + \beta|2p^5 3d^5 L^-\rangle$), the radial integrals (F^k, G^k, and ζ_{3d}) are reduced from their atomic values by the same factor as for the initial state. The ζ_{2p} integral is adjusted to reproduce the experimental energy separation between L_3 and L_2 edges.

For the ligand field part in C_{3v} symmetry, a set of starting parameters was firstly determined by fitting the eigenenergies calculated using the multiconfigurational*ab initio* NEVPT2(9,12) calculation. Secondly, the parameters were adjusted to yield the best agreement between the LFM calculated and experimental XAS/XMCD spectra. All parameters are reported Table 2.

Table 2: Parameters used for the initial Hamiltonian ($\alpha|2p^6 3d^5\rangle + \beta|2p^6 3d^4 L^-\rangle$) and the core-hole final Hamiltonian ($\alpha|2p^5 3d^6\rangle + \beta|2p^5 3d^5 L^-\rangle$) used in the LFM calculations in C_{3v} symmetry. Units are eV. (*) The ligand field and MLCT parameters are chosen equal for initial and excited states.

Atomic parameters							
Initial	$F^2(d,d)$	$F^4(d,d)$	ζ_{3d}				
	9.13	4.94	0.05				
Final	$F^2(d,d)$	$F^4(d,d)$	ζ_{3d}	$F^2(p,d)$	$G^4(p,d)$	$G^3(d,d)$	ζ_{2p}
	9.72	5.26	0.06	5.65	4.22	2.40	8.40
Ligand field and MLCT parameters*							
	$10Dq$	$D\sigma$	$D\tau$	Δ	$V_{e(e_g)}$	$V_{a_1(t_{2g})}$	$V_{e(t_{2g})}$
	4.27	0.01	0.002	4.0	1.2	0.1	0

All quantities (magnetic moments and spectra) were computed for a powder sample using the Lebedev quadrature (see Methods). The spin, orbital, and total magnetic moments at 6.5 T and 2 K for the powder $K_3[Fe^{III}(CN)_6]$ are reported in Table 1. The calculated XAS/XMCD spectra are compared to the experimental spectra in Figure 2 and compared to the two other low-spin Fe(III) compounds. For Fe^{III}Tp, the experimental and calculated XAS and XMCD spectra are taken from our previous work[32] where the calculation was done in C_{3v} symmetry with MLCT. For $Fe^{III}(tacn)_2$ we calculated the XAS and XMCD spectra starting with the crystal field parameters from reference[60] and including a slight C_{3v} distortion. In this case, no MLCT is needed and a good agreement between the experiment and calculations was obtained.

4 Discussion

In the previous section, we reported the powder XAS and XMCD spectra as well as other quantities such as the spin and orbital angular momenta of a powder $K_3[Fe^{III}(CN)_6]$ sample. The good agreement between experiments and LFM calculations confirms that the crystal field parameters and MLCT parameters from Table 2 describe correctly the initial state. The experimental data were obtained on powders whereas the LFM calculations and the multiconfigurational *ab initio* calculations were performed on oriented clusters. Great care

was taken to average the theoretical angular dependencies so that calculations can be compared to experiments. In the present section, we take complete advantage of the calculations on oriented clusters in order to check the magnetic anisotropies firstly at the level of one $Fe(CN)_6$ cluster, and secondly on an oriented unit cell of $K_3[Fe^{III}(CN)_6]$. Thirdly we check what is the sensitivity of the powder spectra to distortions.

4.1 Magnetic anisotropy of the isolated $Fe(CN)_6$ cluster

In this section, we focus on the magnetic anisotropy of one $Fe(CN)_6$ cluster of the multiconfigurational *ab initio* calculations at 2 K in a 6.5 T external induction.

In Figure 4, the spin, orbital, and total magnetic moments are plotted as a function of the unit sphere (θ, ϕ) coordinates.[90] The three-dimensional representations of the magnetic moments (called *magnetic distribution* in the following) are far from spherical. In literature, the spatial magnetic properties of tensors such as the Landé gyromagnetic tensor g or the magnetic susceptibility χ are represented by ellipsoids for which only three values are needed to construct all the angular dependencies.[55] These are 2-dimensional, rank 3 Cartesian tensors, *i.e* with 9 components. In the present case, one sees that the exact angular dependence of $\langle L_{\hat{k}} \rangle$ and $\langle S_{\hat{k}} \rangle$ cannot be described by an ellipsoid. $\langle L_{\hat{k}} \rangle$ has the shape of a capsule whereas $\langle S_{\hat{k}} \rangle$ has the shape of a peanut. The main difference between capsule and peanut shapes is that for the peanut shape, the spin magnetic moment is almost equal to zero in one specific direction whereas it remains finite in all directions for the capsule shape of the orbit magnetic moment. The particular directions of magnetization can then be determined. The *magnetic distributions* indicate the presence of an easy axis of magnetization (direction for which the total magnetic moment is the largest). We label this direction $\hat{u}_1$, that has for spherical coordinates ($\theta = 58.5°, \phi = -10.6°$) in the $\{\hat{x}, \hat{y}, \hat{z}\}$ crystal frame. It can be noticed that the $\hat{u}_1$ direction is the same for the orbital, spin and total magnetic moments and that it points roughly along the pseudo-C_3 axis.

In addition to $\hat{u}_1$, we define two other axes ($\hat{u}_2$, $\hat{u}_3$) that guide our understanding of the

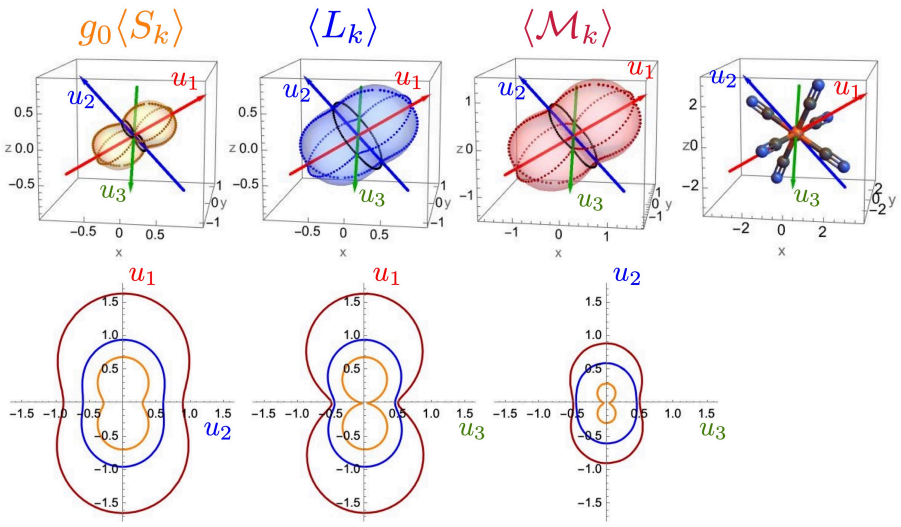

Figure 4: (*Top*) *Magnetic distributions* from multiconfigurational *ab initio* calculation for $K_3[Fe^{III}(CN)_6]$ at 2 K and 6.5 T in the $\{\hat{x}, \hat{y}, \hat{z}\}$ crystal frame (units are μ_B): $g_0\langle S_{\hat{k}}\rangle$ (transparent yellow) where $g_0 \approx 2$, $\langle L_{\hat{k}}\rangle$ (transparent blue) and $\langle \mathcal{M}_{\hat{k}}\rangle$ (transparent red). The easy magnetization axis, u_1 , is indicated by the red arrow, u_2 by the blue arrow and u_3 by the green arrow (direction of the minimum of magnetization). The $Fe(CN)_6$ cluster is represented in the right-top panel in the crystal frame. *(Bottom)* Cut of the *magnetic distributions* along the (u_1, u_2), (u_1, u_3) and (u_2, u_3) planes: $g_0\langle S_{\hat{k}}\rangle$ (–), $\langle L_{\hat{k}}\rangle$ (–), $\langle \mathcal{M}_{\hat{k}}\rangle$ (–).

magnetic anisotropy ($\hat{u}_i$ are unit vectors): $\hat{u}_3$ is the direction perpendicular to $\hat{u}_1$ for which the magnetic moment is the smallest. $\hat{u}_2$ is the direction perpendicular to $\hat{u}_1$ for which the magnetic moment is the largest (see Figure 4). Although this is not exactly compulsory by construction, one observes that $\hat{u}_2$ is almost perpendicular to $\hat{u}_3$ so that ($\hat{u}_1$, $\hat{u}_2$, $\hat{u}_3$) is close to an orthonormal frame. The Cartesian coordinates of $\hat{u}_1$, $\hat{u}_2$, $\hat{u}_3$ in the crystal frame are given in SI (Table S5). In order to illustrate the magnetic distribution, we also plotted cuts in the $(\hat{u}_1, \hat{u}_2)$, $(\hat{u}_1, \hat{u}_3)$ and $(\hat{u}_2, \hat{u}_3)$ planes. The values are obtained within the 385-point Lebedev grid so that the determination of the ($\hat{u}_1$, $\hat{u}_2$, $\hat{u}_3$) directions is slightly complicated by the discrete nature of the grid but a large number of grid points ensures that the errors are limited, below 7°. The *ab initio magnetic distributions* can be compared to the LFM calculations in SI (Figure S5) where $\langle T_{\hat{k}}\rangle$ is also plotted. As expected from the imposed

C_{3v} symmetry, the three different *magnetic distributions* present a revolution axis along the C_3 direction. Consistent with the *ab initio* multiconfigurational calculation, the *magnetic distributions* have all an easy axis of magnetization along the C_3 axis and a plane of hard magnetization perpendicular to the C_3 axis. In the plane of hard magnetization, the curves of the *magnetic distributions* obtained from LFM calculation are circles whereas dumbbells-like in the multiconfigurational *ab initio* calculation.

For comparison, the *magnetic distribution* for $Fe^{III}Tp$ from multiconfigurational *ab initio* calculation is presented in Figure 5. The ($\hat{u}_1$, $\hat{u}_2$, $\hat{u}_3$) axes were also determined using the previous definitions. The magnetic anisotropy for $K_3[Fe^{III}(CN)_6]$ differs from the one observed for $Fe^{III}Tp$. In the case of $K_3[Fe^{III}(CN)_6]$, the orbital magnetic moment dominates the spin magnetic moment for all directions, *i.e.* $\langle L_{\hat{k}} \rangle > g_0 \langle S_{\hat{k}} \rangle$ for all $\hat{k}$. For FeTp, $\langle L_{\hat{k}} \rangle$ is larger than $g_0 \langle S_{\hat{k}} \rangle$ in most directions except for some of them, for instance in the $(\hat{u}_2, \hat{u}_3)$ plane (Figure 5). In addition, one also notices that the $\langle L_{\hat{k}} \rangle$ is never quenched for $K_3[Fe^{III}(CN)_6]$ (it is larger than $0.45\mu_B$) whereas it is almost completely quenched in the $(\hat{u}_2, \hat{u}_3)$ plane for $Fe^{III}Tp$. The situation for the spin magnetic moments is different since they are almost similar for the two compounds.

4.1.1 The effect of the spin-orbit coupling on the magnetic anisotropy

We explored the impact of the spin-orbit coupling on the magnetic properties of one isolated $Fe(CN)_6$ cluster. The calculations were conducted within the LFM theory in the C_{3v} symmetry where it is easy to switch on or off the spin-orbit coupling and adjust the intensity of the external magnetic induction between 6.5 T and 0.1 T. The calculated *magnetic distributions* are reported in Figure 6.

As can be seen in Figure 6, the presence of spin-orbit coupling has a strong influence on the spin magnetic moment since it drastically modifies the shape of the *spin magnetic distributions*, going from an almost perfect sphere for ζ_{3d} = 0 to a peanut shape when ζ_{3d} = 0.05 eV. The impact of the spin-orbit coupling is not as large for the orbital magnetic

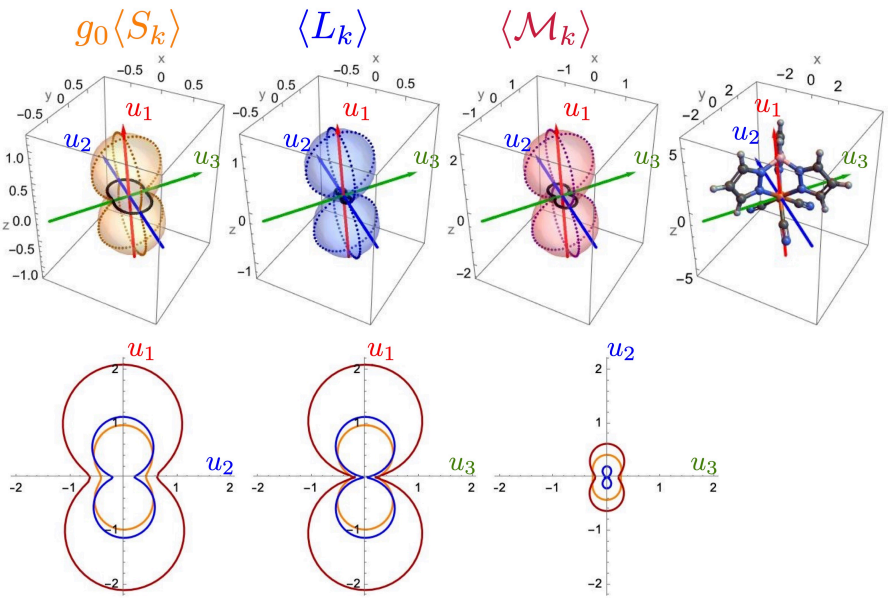

Figure 5: (*Top*) *Magnetic distributions* from multiconfigurational *ab initio* calculation for $Fe^{III}Tp$ at 2 K and 6.5 T in the $\{\hat{x}, \hat{y}, \hat{z}\}$ crystal frame (units are μ_B): $g_0\langle S_{\hat{k}}\rangle$ (transparent yellow) where $g_0 \approx 2$, $\langle L_{\hat{k}}\rangle$ (transparent blue) and $\langle \mathcal{M}_{\hat{k}}\rangle$ (transparent red). The easy magnetization axis, u_1 , is indicated by the red arrow, u_2 by the blue arrow and u_3 by the green arrow. The $Fe^{III}Tp$ cluster is represented in the right-top panel in the crystal frame. *(Bottom)* Cut of the *magnetic distributions* along the (u_1, u_2), (u_1, u_3) and (u_2, u_3) planes: $g_0\langle S_{\hat{k}}\rangle$ (–), $\langle L_{\hat{k}}\rangle$ (–), $\langle \mathcal{M}_{\hat{k}}\rangle$ (–).

moment, since it has a peanut shape in a small magnetic field and $\zeta_{3d} = 0$. In the presence of a large magnetic field, the shape of the orbital magnetic moment transforms into a capsule. To quantify the anisotropy of spin and orbit *magnetic distributions*, we define a sphericity parameter $\mathcal{R}_{O_{\hat{k}}} = Min(|\langle O_{\hat{k}}\rangle|)/Max(|\langle O_{\hat{k}}\rangle|) = |\langle O_{\hat{u}_3}\rangle|/|\langle O_{\hat{u}_1}\rangle|$ where $O_{\hat{k}} = S_{\hat{k}}$ for the spin and $O_{\hat{k}} = L_{\hat{k}}$ for the orbit. The sphericity values are reported in Table 3. In the absence of spin-orbit coupling, one expects no impact of the crystal field on the spin magnetic moment and a finite impact on the orbital magnetic moment. Indeed, we find $\mathcal{R}_{L_{\hat{k}}} \approx 0$ and $\mathcal{R}_{S_{\hat{k}}} \approx 1$ in a magnetic field as small as 0.1 T. In a larger magnetic field (6.5 T), the spin magnetic distribution remains spherical ($\mathcal{R}_{S_{\hat{k}}} \approx 1$) whereas the orbital magnetic anisotropy is slightly decreased but almost null ($\mathcal{R}_{L_{\hat{k}}} \leq 0.01$).

In the presence of spin-orbit coupling, a part of the orbital magnetic anisotropy is trans-

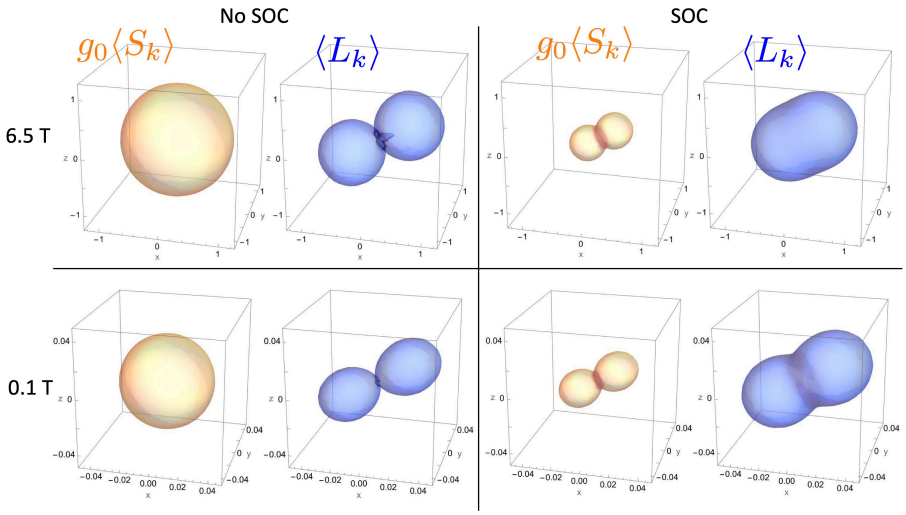

Figure 6: *Magnetic distributions* for the spin ($g_0\langle S_{\hat{k}}\rangle$ in yellow, $g_0 \approx 2$) and orbit ($\langle L_{\hat{k}}\rangle$ in blue) calculated with Quanty for $K_3[Fe^{III}(CN)_6]$ at 2 K: in 0.1 T (bottom row) and 6.5 T (top row) external magnetic induction, without (left column) and with (right column) spin-orbit coupling (labeled SOC). Units are μ_B.

Table 3: LFM calculation of the sphericity for the spin, orbital, and total magnetic moments for the powder, calculated at 2 K, 0.1 T and 6.5 T, with and without spin-orbit coupling (labeled SOC), compared with the multiconfigurational *ab initio* calculation (with spin-orbit). The $\mathcal{R}$ values are unitless and the magnetic moments in μ_B.

	LFM				*Ab initio*	
	no SOC		SOC		SOC	
	0.1 T	6.5 T	0.1 T	6.5 T	0.1 T	6.5 T
$\mathcal{R}_{S_{\hat{k}}}$	1.0	1.0	0.2	0.3	0.0	0.1
$\mathcal{R}_{L_{\hat{k}}}$	0.0	0.0	0.4	0.7	0.2	0.5
$g_0\langle S_{\hat{k}}\rangle_{powder}$	−0.03	−0.98	−0.02	−0.37	−0.02	−0.39
$\langle L_{\hat{k}}\rangle_{powder}$	−0.02	−0.56	−0.03	−0.79	−0.03	−0.69
$\langle \mathcal{M}_{\hat{k}}\rangle_{powder}$	0.05	1.54	0.05	1.16	0.04	1.08

ferred to the spin magnetic distribution, so that both *magnetic distributions* adopt a peanut shape. This is best seen in a small magnetic field, where $\mathcal{R}_{L_{\hat{k}}} \approx 0.4$ (spin-orbit on) compared to $\mathcal{R}_{L_{\hat{k}}} \approx 0.0$ (spin-orbit off), and $\mathcal{R}_{S_{\hat{k}}} \approx 0.2$ (spin-orbit on) compared to $\mathcal{R}_{S_{\hat{k}}} \approx 1$ (spin-orbit off). With a larger magnetic field of 6.5 T, the sphericity for both spin and orbital magnetic

distributions increase, since $\mathcal{R}_{L_{\hat{k}}} \approx 0.7$ and $\mathcal{R}_{S_{\hat{k}}} \approx 0.3$. One can notice that the orbital magnetic distribution takes the shape of a capsule when the magnetic field is large whereas the spin magnetic distribution remains with a peanut shape. In the present case, the anisotropy transfer from the orbital magnetic moment to the spin magnetic moment is all the more effective as the orbital magnetic moment is large and dominates the spin magnetic moment.

The multiconfigurational *ab initio* calculated sphericity values, obtained using the crystallographic structure and including spin-orbit, are also given in Table 3 at 0.1 T and 6.5 T (detailed in SI S3). Although the *ab initio* results are not identical to the LFM calculations performed in C_{3v} symmetry, the general trend is rather similar. Additional results from the LFM and the *ab initio* calculations are given in SI (Table S4): minimum and maximum values of the magnetic moments with their sphericity factors, and powder values.

When the spin-orbit coupling is off, the spin magnetic moment of the powder in a 6.5 T magnetic induction is close to 1 μ_B, that is the value expected for a pure ($S = 1/2$, $m_S = -1/2$) state (Table 3), and the orbital magnetic moment remains high but lower than the spin magnetic moment. The spin-orbit coupling drastically reduces the spin magnetic moment by a factor greater than two and increases the orbital magnetic moment so that it is larger than the spin magnetic moment. The spin magnetic anisotropy is thus influenced by the orbital magnetic anisotropy as pointed out in the analysis of the *magnetic distributions*.

4.1.2 The effect of crystal field symmetry on the magnetic anisotropy

Following the above LFM analysis performed in C_{3v} symmetry, we explored the impact of symmetry by performing multiconfigurational *ab initio* calculations using the symmetrized molecule in C_{3v}, D_{4h} and O_h symmetries (see section 3.3) in a 6.5 T external magnetic induction. One first observes that the energies of the three Kramers doublets calculated with the C_{3v} symmetry are in much better agreement with the values determined from the exact C_1 symmetry than the energies determined by the calculations in D_{4h} and O_h symmetry (see S2 in SI).

The powder values of the magnetic moments calculated at 6.5 T and 2 K, their minimum and maximum values, and the sphericity factors are reported in SI (Table S3) for the different symmetries. The spin and orbital magnetic moments calculated for the powder have almost the same values for all symmetries, although differences are observed in the *magnetic distribution*. In O_h symmetry, $\mathcal{R}_{S_{\hat{k}}}$ and $\mathcal{R}_{L_{\hat{k}}}$ are close to 1 as could be expected for a cubic point group. Surprisingly, the sphericity remains quite high in D_{4h} symmetry since both $\mathcal{R}_{S_{\hat{k}}}$ and $\mathcal{R}_{L_{\hat{k}}}$ are larger than 0.9, much higher than the sphericity values calculated for C_{3v} symmetry ($\mathcal{R}_{S_{\hat{k}}} = 0.4, \mathcal{R}_{L_{\hat{k}}} = 0.7$). In addition, for D_{4h} symmetry, the easy magnetization axis is along the C_4 axis, *i.e.* along the apical C−Fe−C bond whereas, for C_{3v} symmetry, it is along the C_3 axis that does not go through any carbon atom of the cyanido ligands and that is very close to pseudo ternary axis of the real molecule. It can then be concluded that a D_{4h} symmetry for the Fe(III) site in $K_3[Fe^{III}(CN)_6]$ fails to mimic the magnetic properties of $K_3[Fe^{III}(CN)_6]$.

4.2 Magnetic anisotropy of the $K_3[Fe^{III}(CN)_6]$ unit cell

From the $K_3[Fe^{III}(CN)_6]$ crystal structure, the unit cell contains four isolated clusters (see Figure 1). Therefore, the magnetic properties of the unit cell must be calculated by summing the single-ion contributions from each of the four Fe(III) ions. In the $P2_1/n$ group, starting from a single Fe(III) ion, the position of the remaining three ions can be obtained by a translation followed by an inversion operation and/or a plane of symmetry (*i.e.* a π rotation followed by an inversion).[67] Some projected views of the cell are proposed in SI to facilitate this description (Figure S3). Orbital and spin magnetic moments are invariant under the inversion (they are even-parity operators) and under translation, so we are simply left with a single π rotation associated with the plane symmetry. Then the contributions from the four Fe(III) ions are reduced to the sum of one Fe(III) ion contribution ($Fe^{III}_{\#1}$) plus its symmetric contribution by a π rotation ($Fe^{III}_{\#2}$) (see Figure 1). This sum has to be doubled to account for the four Fe(III) ions in the unit cell.

Applying these symmetry properties, we calculated the *magnetic distributions* of the total magnetic moment, $\mathcal{M}^{total}$ of the four Fe^{III} ions in the unit cell. The easy axis directions is $(\theta = 58.5°, \phi = -10.6°)$ for $Fe^{III}_{\#1}$ and $(\theta = 58.5°, \phi = 10.6°)$ for $Fe^{III}_{\#2}$. Thus, the easy axis directions of the two Fe(III) sites make an angle of approximately 18°. The calculated *magnetic distributions* resulting from four Fe(III) ions in the crystal unit cell are plotted in SI (Figure S4). They evidence an easy magnetization axis in the $\hat{v}_1$ direction $(\theta = 57.75°, \phi = 0°)$, and a hard plane of magnetization perpendicular to $\hat{v}_1$. Coordinates of the special magnetization directions ($\hat{v}_1$, $\hat{v}_2$, $\hat{v}_3$) are given in SI (Table S6). In the easy magnetization direction, the magnetic moments take the maximum values: $\mathcal{M}^{total}_{max} = 4 \times 1.62\mu_B$ ($\mathcal{M}^{spin}_{max} = 4 \times 0.68\mu_B$ and $\mathcal{M}^{orbit}_{max} = 4 \times 0.94\mu_B$). If renormalized to one Fe(III) ion, $\mathcal{M}^{total}_{max}$ is only slightly smaller than the one site value ($\mathcal{M}^{total}_{max} = 1.64\mu_B$) (see Table S4). The minimum magnetization is $\mathcal{M}^{total}_{min} = 4 \times 0.62\mu_B$ ($\mathcal{M}^{spin}_{min} = 4 \times 0.12\mu_B$ and $\mathcal{M}^{orbit}_{min} = 4 \times 0.50\mu_B$).

From the above analysis, it is possible to compute the angular dependencies of the XAS, XNLD, and XMCD signals in a unit cell. These spectra are the ones that could be measured if the experiments could be performed on a $K_3[Fe^{III}(CN)_6]$ single crystal. The spectra were calculated in the LFM model for the $Fe(CN)_6$ cluster with C_{3v} symmetry, where the C_3 axis is parallel to the easy magnetization axis, *i.e.* $\hat{u}_1$ direction. We computed the XAS, XNLD, and XMCD signals for four different Fe(III) ions with the C_3 axes making the angles $(\theta = 58.5°, \phi = 10.6°)$ for two of them and the angle $(\theta = 58.5°, \phi = -10.6°)$ for the other two. The XNLD intensity is very small due to the small distortion and represents only 0.1 % of the isotropic spectrum. From the multiconfigurational *ab initio* calculation, we know that the easy magnetization axis of the unit cell points in the $\hat{v}_1(\theta = 57.75°, \phi = 0°)$ direction so we calculated σ_{XMCD} for either $\hat{k} \parallel \hat{v}_1$ or $\hat{k} \perp \hat{v}_1$ (see Figure 7).

4.3 Magnetic properties of the $K_3[Fe^{III}(CN)_6]$ powder

In the two previous sections, we observed that large magnetic anisotropies were present for each Fe(III) ion of $K_3[Fe^{III}(CN)_6]$. These anisotropies remain though partially reduced when

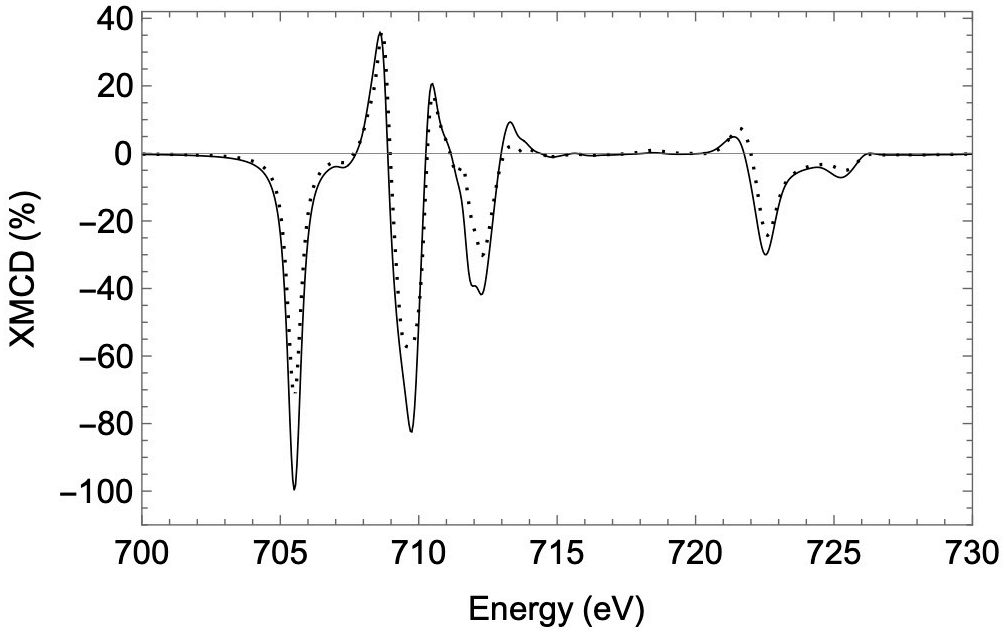

Figure 7: XMCD angular dependence calculated for the unit cell in the LFM model, with $\hat{k} \parallel \hat{v}_1$ (line) and $\hat{k} \perp \hat{v}_1$ (dotted line), $\hat{v}_1$ being the easy magnetization axis of the unit cell. XMCD is given in percent of the maximum of the XAS (at 710.2 eV).

the unit cell with four Fe(III) ions is considered. From the theoretical analyses performed within the multiconfigurational *ab initio* framework or from the LFM framework, the role played by the various ingredients of the Hamiltonian (spin-orbit coupling, crystal-field, site symmetry, external magnetic field) was fully explored. Obviously, dealing with perfect powders, all the magnetic anisotropies disappear and the impact of the Hamiltonian parameters needs to be explored. This is what is done in the present section where one finds the signature of the Hamiltonian parameters on the XAS and XMCD signals for a powder.

4.3.1 π back-bonding and MLCT

The π back-bonding effect can be examined through the LFM calculations by comparing calculations with or without MLCT. In the case of $K_3[Fe^{III}(CN)_6]$, one observes that the MLCT has little effect on the average magnetic moments that increase by less than 1%. In the case of $Fe^{III}Tp$, the magnetic moment is decreased by 3% for the orbit and by 13% for

the spin. Since $K_3[Fe^{III}(CN)_6]$ is surrounded by six CN ligands whereas $Fe^{III}Tp$ by three, one would expect a more important MLCT effect for $K_3[Fe^{III}(CN)_6]$. In contrast, the MLCT has a strong effect on the XAS and XMCD spectral shapes as can be seen from the experimental and LFM calculated spectra (Figure 2). This was previously pointed at for XAS by Hocking *et al.* who performed a D_{4h} calculation. The MLCT creates a large splitting of the states, visible in the transitions in the 711-715 eV energy range at the L_3 edge and 724-725 eV energy range at the L_2 edge. But it hardly changes the integrated XAS and XMCD spectra, leading to almost unchanged magnetic moments when applying the sum rules. The case of low spin Fe(III) with no π back-bonding can be illustrated with the compound $Fe^{III}(tacn)_2$. In this case, no MLCT is needed in the LFM calculations to obtain a good agreement with the experimental spectra (Figure 2).

4.3.2 Local distortions and magnetic properties of a powder

From the sections above, we noticed that the small distortions around the Fe(III) site have almost no impact on the average properties of a powder, whereas they play an important role in their angular dependencies. We have calculated the magnetic properties by taking the exact environment for the Fe(III) ion or approximated C_{3v}, D_{4h}, and O_h symmetries. The distortion and the site symmetry have almost no impact on the average total magnetic moments: $\mathcal{M}^{total}$ = 1.079μ_B in O_h and D_{4h} symmetries, 1.078μ_B in C_{3v} and 1.075μ_B in C_1 exact symmetry (orbit and spin magnetic moments reported in SI Table S3).

The XAS and XMCD spectra for a powder were calculated within the LFM framework for O_h, D_{4h}, and C_{3v} site symmetries. The spectra calculated for the three different symmetries are similar except for a small feature at 718.5 eV in the XMCD signal. For the O_h symmetry, the feature is absent since it is forbidden as explained by Hocking *et al.*[39] For the D_{4h} symmetry, the XMCD feature is negative, whereas it is positive with the C_{3v} symmetry calculation and for the experiment.

5 Conclusion

In this work, we have investigated the local magnetic properties of the d^5 low spin $K_3[Fe^{III}(CN)_6]$ compound in the randomly oriented powder form. We combined SQUID magnetometry and XMCD spectroscopy for the experiments that were analyzed by both molecular multiconfigurational *ab initio* and atomic ligand field multiplets calculations. XMCD technique offers a direct measurement of the orbit magnetic moment and completes the previous work by Figgis and Day *et al.* on ferricyanide using spin-polarized neutron diffraction experiments,[26] whereas the SQUID magnetometry gives the total magnetic moment. In order to get theoretical values for the powder, we calculated the orbit and spin magnetic moments as a function of the magnetic induction in the $K_3[Fe^{III}(CN)_6]$ cluster and the angular dependencies were averaged. We also calculated the XAS/XMCD spectra. Thus a detailed analysis of the magnetic anisotropies was done.

The main result is that the orbit magnetic moment dominates the spin magnetic moment ($\mathcal{M}_{orbit}^{powder} > \mathcal{M}_{spin}^{powder}$), in the case of the powder. An orbit magnetic moment greater than the spin magnetic moment is exceptional for $3d$ transition metal ions and seems to only occur in d^5 low spin Fe(III) compounds.[26,32] Moreover, the calculations determined that this property holds for all directions of the magnetic induction. This differs from the case of low spin $Fe^{III}Tp$ compound where $\mathcal{M}_{orbit}^{powder} \leq \mathcal{M}_{spin}^{powder}$ in some particular directions of the magnetic induction.

A second main result from calculations is that $Fe(CN)_6$ cluster has an easy magnetization axis in the direction of the pseudo-C_{3v} axis. In the unit cell with four Fe(III) sites, the anisotropy is partially reduced and the crystal easy axis of magnetization points in the (a, c) plane.

A third main result shows that the spin-orbit coupling when combined with a large crystal field plays a major role in the magnetic properties since it transfers the anisotropy of the orbit magnetic moment to the spin magnetic moment and the transfer is all the more effective than the orbit magnetic moment is large and dominates the spin magnetic moment for any

direction of the external magnetic induction.

A minor result concerns the approximative symmetry used in LFM calculation. Among several possible geometries such as O_h, D_{4h} and C_{3v} tested in the multiconfigurational *ab initio* calculations, it was found that the C_{3v} symmetrization was a good compromise yielding essentially the same electronic structure and magnetic anisotropies as the ones computed from the exact geometry.

In the domain of molecular magnetism, $K_3[Fe^{III}(CN)_6]$ is used as a building block in *Prussian blue* analogs, and the present analysis might open new insight into the interpretation of the magnetic properties of this widely used class of materials.

Acknowledgement

This work was supported by the Centre National de la Recherche Scientifique (CNRS, France), the Ministère de l'Enseignement Supérieur et de la Recherche (MESR, France), and the GDR MCM-2 French research group. The authors acknowledge SOLEIL for the provision of synchrotron radiation facilities through proposal 99130220, the DEIMOS beamline staff for technical and scientific support during experiments, and Loïc Joly (IPCMS) for computing support at DEIMOS. We thank Lorenzo Paulatto (IMPMC) for computing support.

Supporting Information Available

Detailed analysis (sum rules) of the experimental XMCD spectra. Details of the Ligand Field Multiplet and multiconfigurational *ab initio* calculations. This material is available free of charge via the Internet at `http://pubs.acs.org/`.

References

(1) Sharpe, A. G. *Chemistry of cyano complexes of the transition metals*; Academic Press, 1976.

(2) Gail, E.; Gos, S.; Kulzer, R.; Lorösch, J.; Rubo, A.; Sauer, M. *Ullmann's Encyclopedia of Industrial Chemistry*; John Wiley and Sons, Ltd, 2004; DOI: https://doi.org/10.1002/14356007.a08_159.pub2.

(3) Kwong, H.-L.; Afonso, C. A. M.; Branco, L. C. *Encyclopedia of Reagents for Organic Synthesis*; John Wiley Sons, Ltd, 2007; DOI: https://doi.org/10.1002/9780470842898.rp213.pub2.

(4) Mateles, R. I. Ferricyanide Reduction Method for Reducing Sugars. *Nature* **1960**, *187*, 241–242, DOI: 10.1038/187241a0.

(5) Pasco, N.; Baronian, K.; Jeffries, C.; Webber, J.; Hay, J. MICREDOX®—development of a ferricyanide-mediated rapid biochemical oxygen demand method using an immobilised Proteus vulgaris biocomponent. *Biosens Bioelectron* **2004**, *20*, 524–532, DOI: 10.1016/j.bios.2004.02.016.

(6) Kraft, A. On the discovery and history of Prussian Blue. *Bulletin for the history of chemistry / Division of the History of Chemistry of the American Chemical Society* **2008**, *33*, 61–67.

(7) Soloveichik, G. L. Flow Batteries: Current Status and Trends. *Chemical Reviews* **2015**, *115*, 11533–11558, DOI: 10.1021/cr500720t.

(8) Hu, M.; Wang, A. P.; Luo, J.; Wei, Q.; Liu, T. L. Cycling Performance and Mechanistic Insights of Ferricyanide Electrolytes in Alkaline Redox Flow Batteries. *Advanced Energy Materials* **2023**, *13*, 2203762, DOI: https://doi.org/10.1002/aenm.202203762.

(9) Sato, O.; Iyoda, T.; Fujishima, A.; Hashimoto, K. Photoinduced Magnetization of a Cobalt-Iron Cyanide. *Science* **1996**, *272*, 704–705, DOI: 10.1126/science.272.5262.704.

(10) Bleuzen, A.; Lomenech, C.; Escax, V.; Villain, F.; Varret, F.; Cartier dit Moulin, C.; Verdaguer, M. Photoinduced ferrimagnetic systems in Prussian Blue Analogues $C^{I}_{x}Co_4[Fe(CN)_6]_y$ (C^{I} = alkali cation). 1. Conditions to observe the phenomenon. *Journal of the American Chemical Society* **2000**, *122*, 6648–6652, DOI: 10.1021/ja000348u.

(11) Escax, V.; Bleuzen, A.; Cartier dit Moulin, C.; Villain, F.; Goujon, A.; Varret, F.; Verdaguer, M. Photoinduced ferrimagnetic systems in Prussian Blue Analogues $C^{I}_{x}Co_4[Fe(CN)_6]_y$ (C^{I} = alkali cation). 3. Control of the photo- and thermally induced electron transfer by the $[Fe(CN)_6]$ vacancies in cesium derivatives. *Journal of the American Chemical Society* **2001**, *123*, 12536–12543, DOI: 10.1021/ja011296r, PMID: 11741417.

(12) Bleuzen, A.; Escax, V.; Ferrier, A.; Villain, F.; Verdaguer, M.; Münsch, P.; Itié, J.-P. Thermally Induced Electron Transfer in a CsCoFe Prussian Blue Derivative: The Specific Role of the Alkali-Metal Ion. *Angew. Chem. Int. Ed.* **2004**, *43*, 3728–3731, DOI: 10.1002/anie.200460086.

(13) Shimamoto, N.; Ohkoshi, S.-i.; Sato, O.; Hashimoto, K. Control of Charge-Transfer-Induced Spin Transition Temperature on Cobalt-Iron Prussian Blue Analogues. *Inorganic Chemistry* **2002**, *41*, 678–684, DOI: 10.1021/ic010915u, PMID: 11849066.

(14) Nihei, M. Molecular Prussian Blue Analogues: From Bulk to Molecules and Low-dimensional Aggregates. *Chem. Lett.* **2020**, *49*, 1206–1215, DOI: 10.1246/cl.200428.

(15) Huang, W.; Ma, X.; Sato, O.; Wu, D. Controlling dynamic magnetic properties of coordination clusters via switchable electronic configuration. *Chem. Soc. Rev.* **2021**, *50*, 6832–6870, DOI: 10.1039/d1cs00101a.

(16) Figgis, B. N. The magnetic properties of transition metal ions in asymmetric ligand fields. Part 2.—Cubic field $^3T_2$ terms. *Trans. Faraday Soc.* **1961**, *57*, 198–203, DOI: 10.1039/tf9615700198.

(17) Jackson, L. The principal magnetic susceptibilities of some paramagnetic crystals at low temperatures. *Proc. R. Soc. London A.* **1933**, *140*, 695–713, DOI: 10.1098/rspa.1933.0097.

(18) McKim, F. R.; Wolf, W. P. The Susceptibility and Magnetic Specific Heat of Potassium Ferricyanide at Low Temperatures. *Proc. Phys. Soc. London, Sect. B* **1956**, *69*, 1231–1236, DOI: 10.1088/0370-1301/69/12/306.

(19) Bleaney, B.; O'Brien, M. C. M. Paramagnetic Resonance in some Complex Cyanides of the Iron Group II. Theory. *Proc. Phys. Soc. London, Sect. B* **1956**, *69*, 1216–1230, DOI: 10.1088/0370-1301/69/12/305.

(20) Baker, J. M.; Bleaney, B.; Bowers, K. D. Paramagnetic Resonance in some Complex Cyanides of the Iron Group I: Experimental Results. *Proc. Phys. Soc. London, Sect. B* **1956**, *69*, 1205–1215, DOI: 10.1088/0370-1301/69/12/304.

(21) Figgis, B. N. The magnetic properties of transition metal ions in asymmetric ligand fields. Part 3.—The behaviour of some t_{2g}^5 complexes. *Trans. Faraday Soc.* **1961**, *57*, 204–209, DOI: 10.1039/tf9615700204.

(22) Rákoš, M.; Varga, Z. Magnetic properties of two complex ferric paramagnetics. *Czech. J. Phys.* **1965**, *15*, 241–250, DOI: 10.1007/bf01689690.

(23) Figgis, B. N.; Gerloch, M.; Mason, R. The crystallography and paramagnetic anisotropy of potassium ferricyanide. *Proceedings of the Royal Society of London. A. Mathematical and Physical Sciences* **1969**, *309*, 91–118, DOI: 10.1098/rspa.1969.0031.

(24) Baker, J.; Figgis, B. N. Magnetic properties of some low-spin iron(III) compounds. *J. Chem. Soc., Dalton Trans.* **1975**, 598, DOI: 10.1039/dt9750000598.

(25) Reschke, R.; Trautwein, A.; Harris, F. E.; Date, S. K. Electronic structure, electron density, electric field gradient-, magnetic susceptability- and G-tensor of $K_3Fe(CN)_6$. *J. Magn. Magn. Mater.* **1979**, *12*, 176–186, DOI: 10.1016/0304-8853(79)90013-1.

(26) Day, P.; Delfs, C. D.; Figgis, B. N.; Reynolds, P. A.; Tasset, F. Polarized neutron diffraction from $Cs_2KFe(CN)_6$. *Mol. Phys.* **1993**, *78*, 769–780, DOI: 10.1080/00268979300100521.

(27) De Groot, F.; Kotani, A. *Core level spectroscopy of solids*; CRC press, 2008.

(28) Beaurepaire, E.; Scheurer, F.; Krill, G.; Kappler, J.-P. *Magnetism and synchrotron radiation*; Springer, 2001; Vol. 34.

(29) Van Bokhoven, J. A.; Lamberti, C. *X-ray absorption and X-ray emission spectroscopy: theory and applications*; John Wiley & Sons, 2016; Vol. 1.

(30) Thole, B. T.; Carra, P.; Sette, F.; van der Laan, G. X-ray circular dichroism as a probe of orbital magnetization. *Phys. Rev. Lett.* **1992**, *68*, 1943–1946, DOI: 10.1103/physrevlett.68.1943.

(31) Carra, P.; Thole, B. T.; Altarelli, M.; Wang, X. X-ray circular dichroism and local magnetic fields. *Phys. Rev. Lett.* **1993**, *70*, 694–697, DOI: 10.1103/physrevlett.70.694.

(32) Jafri, S. F.; Koumousi, E. S.; Sainctavit, P.; Juhin, A.; Schuler, V.; Bunău, O.; Mitcov, D.; Dechambenoit, P.; Mathonière, C.; Clérac, R.; Otero, E.; Ohresser, P.; Cartier dit Moulin, C.; Arrio, M.-A. Large Orbital Magnetic Moment Measured in the $[TpFe^{III}(CN)_3]^-$ Precursor of Photomagnetic Molecular Prussian Blue Analogues. *Inorg. Chem.* **2016**, *55*, 6980–6987, DOI: 10.1021/acs.inorgchem.6b00664.

(33) van der Laan, G.; Zaanen, J.; Sawatzky, G. A.; Karnatak, R.; Esteva, J. M. Comparison of x-ray absorption with x-ray photoemission of nickel dihalides and NiO. *Physical Review B* **1986**, *33*, 4253–4263, DOI: 10.1103/PhysRevB.33.4253.

(34) van der Laan, G.; Thole, B. T. Strong magnetic x-ray dichroism in 2p absorption spectra of 3d transition-metal ions. *Phys. Rev. B* **1991**, *43*, 13401–13411, DOI: 10.1103/physrevb.43.13401.

(35) van der Laan, G.; Kirkman, I. W. The 2p absorption spectra of 3d transition metal compounds in tetrahedral and octahedral symmetry. *Journal of Physics: Condensed Matter* **1992**, *4*, 4189, DOI: 10.1088/0953-8984/4/16/019.

(36) de Groot, F. M. F.; Fuggle, J. C.; Thole, B. T.; Sawatzky, G. A. 2p x-ray absorption of 3d transition-metal compounds: An atomic multiplet description including the crystal field. *Phys. Rev. B* **1990**, *42*, 5459–5468, DOI: 10.1103/physrevb.42.5459.

(37) Arrio, M.-A.; Sainctavit, P.; Cartier dit Moulin, C.; Mallah, T.; Verdaguer, M.; Pellegrin, E.; Chen, C. T. Characterization of Chemical Bonds in Bimetallic Cyanides Using X-ray Absorption Spectroscopy at $L_{2,3}$ Edges. *JACS* **1996ca**, *118*, 6422–6427, DOI: 10.1021/ja9542698.

(38) Arrio, M.-A.; Scuiller, A.; Sainctavit, P.; Cartier dit Moulin, C.; Mallah, T.; Verdaguer, M. Soft X-ray Magnetic Circular Dichroism in Paramagnetic Systems: Element-Specific Magnetization of Two Heptanuclear Cr^{III} $M^{II}{}_6$ High-Spin Molecules. *JACS* **1999**, *121*, 6414–6420, DOI: 10.1021/ja983521j.

(39) Hocking, R. K.; Wasinger, E. C.; de Groot, F. M. F.; Hodgson, K. O.; Hedman, B.; Solomon, E. I. Fe L-Edge XAS Studies of $K_4[Fe(CN)_6]$ and $K_3[Fe(CN)_6]$: A Direct Probe of Back-Bonding. *JACS* **2006**, *128*, 10442–10451, DOI: 10.1021/ja061802i.

(40) Haverkort, M. W.; Zwierzycki, M.; Andersen, O. K. Multiplet ligand-field theory using Wannier orbitals. *Phys. Rev. B* **2012**, *85*, 165113, DOI: 10.1103/PhysRevB.85.165113.

(41) Novák, P.; Knížek, K.; Kuneš, J. Crystal field parameters with Wannier functions: Application to rare-earth aluminates. *Phys. Rev. B* **2013**, *87*, 205139, DOI: 10.1103/PhysRevB.87.205139.

(42) Ramanantoanina, H.; Daul, C. A non-empirical calculation of 2p core-electron excitation in compounds with 3d transition metal ions using ligand-field and density functional theory (LFDFT). *Phys. Chem. Chem. Phys.* **2017**, *19*, 20919–20929, DOI: 10.1039/C7CP03140H.

(43) Gorelov, E.; Guda, A.; Soldatov, M.; Guda, S.; Pashkov, D.; Tanaka, A.; Lafuerza, S.; Lamberti, C.; Soldatov, A. MLFT approach with p-d hybridization for ab initio simulations of the pre-edge XANES. *Radiation Physics and Chemistry* **2020**, *175*, 108105, DOI: https://doi.org/10.1016/j.radphyschem.2018.12.025, 17th International Conference on X-ray Absorption Fine Structure - XAFS2018.

(44) Hariki, A.; Winder, M.; Uozumi, T.; Kuneš, J. LDA + DMFT approach to resonant inelastic x-ray scattering in correlated materials. *Phys. Rev. B* **2020**, *101*, 115130, DOI: 10.1103/PhysRevB.101.115130.

(45) Kuzian, R. O.; Janson, O.; Savoyant, A.; van den Brink, J.; Hayn, R. Ab initio based ligand field approach to determine electronic multiplet properties. *Phys. Rev. B* **2021**, *104*, 085154, DOI: 10.1103/PhysRevB.104.085154.

(46) Kas, J. J.; Rehr, J. J.; Devereaux, T. P. Ab Initio Multiplet-Plus-Cumulant Approach for Correlation Effects in X-Ray Photoelectron Spectroscopy. *Phys. Rev. Lett.* **2022**, *128*, 216401, DOI: 10.1103/PhysRevLett.128.216401.

(47) Krüger, P. First-Principles Calculation of Ligand Field Parameters for L-Edge Spectra of Transition Metal Sites of Arbitrary Symmetry. *Symmetry* **2023**, *15*, DOI: 10.3390/sym15020472.

(48) Josefsson, I.; Kunnus, K.; Schreck, S.; Föhlisch, A.; de Groot, F.; Wernet, P.; Odelius, M. Ab Initio Calculations of X-ray Spectra: Atomic Multiplet and Molecular Orbital Effects in a Multiconfigurational SCF Approach to the L-Edge Spectra of Transition Metal Complexes. *The Journal of Physical Chemistry Letters* **2012**, *3*, 3565–3570, DOI: 10.1021/jz301479j.

(49) Kunnus, K.; Josefsson, I.; Schreck, S.; Quevedo, W.; Miedema, P. S.; Techert, S.; de Groot, F. M. F.; Odelius, M.; Wernet, P.; Föhlisch, A. From Ligand Fields to Molecular Orbitals: Probing the Local Valence Electronic Structure of Ni^{2+} in Aqueous Solution with Resonant Inelastic X-ray Scattering. *The Journal of Physical Chemistry B* **2013**, *117*, 16512–16521, DOI: 10.1021/jp4100813.

(50) Roemelt, M.; Maganas, D.; DeBeer, S.; Neese, F. A combined DFT and restricted open-shell configuration interaction method including spin-orbit coupling: Application to transition metal L-edge X-ray absorption spectroscopy. *The Journal of Chemical Physics* **2013**, *138*, DOI: 10.1063/1.4804607, 204101.

(51) Pinjari, R. V.; Delcey, M. G.; Guo, M.; Odelius, M.; Lundberg, M. Restricted active space calculations of L-edge X-ray absorption spectra: From molecular orbitals to multiplet states. *J. Chem. Phys.* **2014**, *141*, 124116, DOI: 10.1063/1.4896373.

(52) Pinjari, R. V.; Delcey, M. G.; Guo, M.; Odelius, M.; Lundberg, M. Cost and sensitivity of restricted active-space calculations of metal L-edge X-ray absorption spectra. *J. Comput. Chem.* **2015**, *37*, 477–486, DOI: 10.1002/jcc.24237.

(53) Kasper, J. M.; Stetina, T. F.; Jenkins, A. J.; Li, X. Ab initio methods for L-edge x-ray absorption spectroscopy. *Chemical Physics Reviews* **2020**, *1*, DOI: 10.1063/5.0029725, 011304.

(54) Maganas, D.; Kowalska, J. K.; Van Stappen, C.; DeBeer, S.; Neese, F. Mechanism of $L_{2,3}$-edge x-ray magnetic circular dichroism intensity from quantum chemical calcula-

tions and experiment—A case study on V^{IV}/V^{III} complexes. *J. Chem. Phys.* **2020**, *152*, 114107, DOI: 10.1063/1.5129029.

(55) Ridier, K.; Mondal, A.; Boilleau, C.; Cador, O.; Gillon, B.; Chaboussant, G.; Le Guennic, B.; Costuas, K.; Lescouëzec, R. Polarized Neutron Diffraction to Probe Local Magnetic Anisotropy of a Low-Spin Fe(III) Complex. *Angew. Chem. Int. Ed.* **2016**, *55*, 3963–3967, DOI: 10.1002/anie.201511354.

(56) Ferlay, S.; Mallah, T.; Ouahès, R.; Veillet, P.; Verdaguer, M. A room-temperature organometallic magnet based on Prussian blue. *Nature* **1995**, *378*, 701–703.

(57) Cartier dit Moulin, C.; Villain, F.; Bleuzen, A.; Arrio, M.-A.; Sainctavit, P.; Lomenech, C.; Escax, V.; Baudelet, F.; Dartyge, E.; Gallet, J.-J.; Verdaguer, M. Photoinduced ferrimagnetic systems in Prussian Blue Analogues $C^{I}_{x}Co_4[Fe(CN)_6]_y$ (C^{I} = alkali cation). 2. X-ray Absorption Spectroscopy of the metastable state. *J. Am. Chem. Soc.* **2000**, *122*, 6653–6658.

(58) Kunnus, K.; Zhang, W.; Delcey, M. G.; Pinjari, R. V.; Miedema, P. S.; Schreck, S.; Quevedo, W.; Schröder, H.; Föhlisch, A.; Gaffney, K. J.; Lundberg, M.; Odelius, M.; Wernet, P. Viewing the Valence Electronic Structure of Ferric and Ferrous Hexacyanide in Solution from the Fe and Cyanide Perspectives. *The Journal of Physical Chemistry B* **2016**, *120*, 7182–7194, DOI: 10.1021/acs.jpcb.6b04751.

(59) Jafri, S. F.; Arrio, M.-A.; Bordage, A.; Moulin, R.; Juhin, A.; Cartier dit Moulin, C.; Otero, E.; Ohresser, P.; Bleuzen, A.; Sainctavit, P. Weak Ferromagnetic Interaction at the Surface of the Ferrimagnetic $Rb_2Co_4[Fe(CN)_6]_{3.3}\cdot 11H_2O$ Photoexcited State. *Inorganic Chemistry* **2018**, *57*, 7610–7619.

(60) Hahn, A. W.; Van Kuiken, B. E.; Chilkuri, V. G.; Levin, N.; Bill, E.; Weyhermüller, T.; Nicolaou, A.; Miyawaki, J.; Harada, Y.; DeBeer, S. Probing the Valence Electronic Structure of Low-Spin Ferrous and Ferric Complexes Using 2p3d Res-

onant Inelastic X-ray Scattering (RIXS). *Inorg. Chem.* **2018**, *57*, 9515–9530, DOI: 10.1021/acs.inorgchem.8b01550.

(61) N'Diaye, A.; Bordage, A.; Nataf, L.; Baudelet, F.; Rivière, E.; Bleuzen, A. Toward Quantitative Magnetic Information from Transition Metal K-Edge XMCD of Prussian Blue Analogs. *Inorganic Chemistry* **2022**, *61*, 6326–6336, DOI: 10.1021/acs.inorgchem.2c00637.

(62) N'Diaye, A.; Bordage, A.; Nataf, L.; Baudelet, F.; Rivière, E.; Bleuzen, A. Interplay between Transition-Metal K-edge XMCD and Magnetism in Prussian Blue Analogs. *ACS Omega* **2022**, *7*, 36366–36378, DOI: 10.1021/acsomega.2c04049.

(63) Wieghardt, K.; Schmidt, W.; Herrmann, W.; Kueppers, H. J. Redox potentials of bis(1,4,7-triazacyclononane complexes of some first transition series metals(II,III). Preparation of bis(1,4,7-triazacyclononane)nickel(III) perchlorate. *Inorg. Chem.* **1983**, *22*, 2953–2956, DOI: 10.1021/ic00162a037.

(64) McCarthy, S. M.; Bove, P. F.; Matthews, D. E.; Akaike, T.; van der Vliet, A. Nitric Oxide Regulation of MMP-9 Activation and Its Relationship to Modifications of the Cysteine Switch. *Biochemistry-us.* **2008**, *47*, 5832–5840, DOI: 10.1021/bi702496v.

(65) Ohresser, P. et al. DEIMOS: A beamline dedicated to dichroism measurements in the 350–2500 eV energy range. *Rev. Sci. Instrum.* **2014**, *85*, 013106, DOI: 10.1063/1.4861191.

(66) Chen, C. T.; Idzerda, Y. U.; Lin, H.-J.; Smith, N. V.; Meigs, G.; Chaban, E.; Ho, G. H.; Pellegrin, E.; Sette, F. Experimental Confirmation of the X-Ray Magnetic Circular Dichroism Sum Rules for Iron and Cobalt. *Phys. Rev. Lett.* **1995**, *75*, 152–155, DOI: 10.1103/physrevlett.75.152.

(67) Morioka, Y.; Toriumi, K.; Ito, T.; Saito, A.; Nakagawa, I. Crystal Structures of the

Room- and Low-Temperature Phases of Monoclinic Potassium Ferricyanide. *J. Phys. Soc. Jpn.* **1985**, *54*, 2184–2189, DOI: 10.1143/jpsj.54.2184.

(68) Klintenberg, M.; Derenzo, S.; Weber, M. Accurate crystal fields for embedded cluster calculations. *Comput. Phys. Commun.* **2000**, *131*, 120–128, DOI: 10.1016/s0010-4655(00)00071-0.

(69) Derenzo, S. E.; Klintenberg, M. K.; Weber, M. J. Determining point charge arrays that produce accurate ionic crystal fields for atomic cluster calculations. *J. Chem. Phys.* **2000**, *112*, 2074–2081, DOI: 10.1063/1.480776.

(70) Bergner, A.; Dolg, M.; Küchle, W.; Stoll, H.; Preuß, H. *Ab initio* energy-adjusted pseudopotentials for elements of groups 13–17. *Mol. Phys.* **1993**, *80*, 1431–1441, DOI: 10.1080/00268979300103121.

(71) Leininger, T.; Nicklass, A.; Küchle, W.; Stoll, H.; Dolg, M.; Bergner, A. The accuracy of the pseudopotential approximation: Non-frozen-core effects for spectroscopic constants of alkali fluorides XF (X = K, Rb, Cs). *Chem. Phys. Lett.* **1996**, *255*, 274–280, DOI: 10.1016/0009-2614(96)00382-x.

(72) Andrienko, G. A. Chemcraft: 1.8 build 622. 2022.

(73) Neese, F. Software update: The ORCA program system—Version 5.0. *WIREs Comput. Mol. Sci.* **2022**, *12*, DOI: 10.1002/wcms.1606.

(74) Perdew, J. P.; Burke, K.; Ernzerhof, M. Generalized Gradient Approximation Made Simple. *Phys. Rev. Lett.* **1996**, *77*, 3865–3868, DOI: 10.1103/physrevlett.77.3865.

(75) Pantazis, D. A.; Chen, X.-Y.; Landis, C. R.; Neese, F. All-Electron Scalar Relativistic Basis Sets for Third-Row Transition Metal Atoms. *J. Chem. Theory Comput.* **2008**, *4*, 908–919, DOI: 10.1021/ct800047t.

(76) Weigend, F.; Ahlrichs, R. Balanced basis sets of split valence, triple zeta valence and quadruple zeta valence quality for H to Rn: Design and assessment of accuracy. *Phys. Chem. Chem. Phys.* **2005**, *7*, 3297, DOI: 10.1039/b508541a.

(77) Weigend, F. Accurate Coulomb-fitting basis sets for H to Rn. *Phys. Chem. Chem. Phys.* **2006**, *8*, 1057, DOI: 10.1039/b515623h.

(78) Heß, B. A.; Marian, C. M.; Wahlgren, U.; Gropen, O. A mean-field spin-orbit method applicable to correlated wavefunctions. *Chem. Phys. Lett.* **1996**, *251*, 365–371, DOI: 10.1016/0009-2614(96)00119-4.

(79) Atanasov, M.; Ganyushin, D.; Sivalingam, K.; Neese, F. In *Structure and Bonding*; Mingos, D. M. P., Day, P., Dahl, J. P., Eds.; Springer Berlin Heidelberg, 2011; Vol. 143; pp 149–220, DOI: 10.1007/430_2011_57.

(80) Angeli, C.; Cimiraglia, R.; Malrieu, J.-P. N-electron valence state perturbation theory: A fast implementation of the strongly contracted variant. *Chem. Phys. Lett.* **2001**, *350*, 297–305, DOI: 10.1016/s0009-2614(01)01303-3.

(81) Angeli, C.; Cimiraglia, R.; Malrieu, J.-P. *n*-electron valence state perturbation theory: A spinless formulation and an efficient implementation of the strongly contracted and of the partially contracted variants. *J. Chem. Phys.* **2002**, *117*, 9138–9153, DOI: 10.1063/1.1515317.

(82) Neese, F. Efficient and accurate approximations to the molecular spin-orbit coupling operator and their use in molecular g-tensor calculations. *J. Chem. Phys.* **2005**, *122*, 034107, DOI: 10.1063/1.1829047.

(83) Haverkort, M. W.; Sangiovanni, G.; Hansmann, P.; Toschi, A.; Lu, Y.; Macke, S. Bands, resonances, edge singularities and excitons in core level spectroscopy investigated within the dynamical mean-field theory. *Europhys. Lett.* **2014**, *108*, 57004, DOI: 10.1209/0295-5075/108/57004.

(84) Haverkort, M. W. Quanty for core level spectroscopy - excitons, resonances and band excitations in time and frequency domain. *J. Phys. Conf. Ser.* **2016**, *712*, 012001, DOI: 10.1088/1742-6596/712/1/012001.

(85) Retegan, M. Crispy: v0.7.3. 2019.

(86) König, E.; Kremer, S. *Ligand Field*; Springer US: Boston, MA, 1977; DOI: 10.1007/978-1-4757-1529-3.

(87) Ayant, Y.; Belorizky, E.; Guillot, M.; Rosset, J. Interprétation de l'aimantation du gallate d'erbium en champ fort et à basse température. *J. Phys.* **1965**, *26*, 385–389, DOI: 10.1051/jphys:01965002607038500.

(88) Piamonteze, C.; Miedema, P.; de Groot, F. M. F. Accuracy of the spin sum rule in XMCD for the transition-metal L edges from manganese to copper. *Phys. Rev. B* **2009**, *80*, 184410, DOI: 10.1103/physrevb.80.184410.

(89) Ashcroft, N. W.; Mermin, N. D. *Solid state physics*; Cengage Learning, 2022.

(90) Wolfram Research, I. Mathematica, Version 13.1. 2022.

Graphical TOC Entry

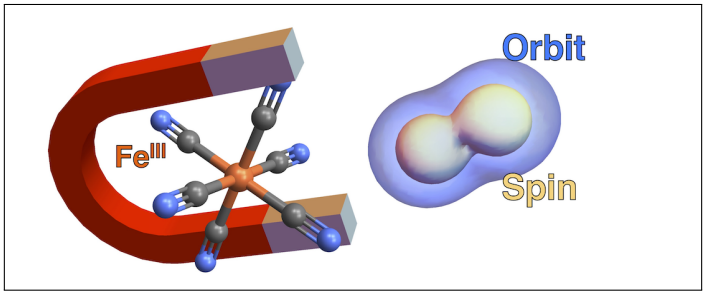

The $K_3[Fe^{III}(CN)_6]$ compound with single low-spin $S = 1/2$ Fe(III) ions was investigated by X-ray magnetic circular dichroism. The electronic and magnetic properties were determined by a combination of multi-configurational *ab initio* and atomic ligand field multiplet calculations. Remarkably, the orbital magnetic moment dominates the spin magnetic moment in all directions of the external magnetic induction, an exceptional property among $3d$ transition metal ions.